MPDATA: Third-order accuracy for variable flows

Maciej Waruszewski[a,*], Christian Kühnlein[b], Hanna Pawlowska[a], Piotr K. Smolarkiewicz[b]

[a] *Institute of Geophysics, Faculty of Physics, University of Warsaw, Warsaw, Poland*
[b] *European Centre for Medium-Range Weather Forecasts, Shinfield Park, Reading, RG2 9AX, United Kingdom*

Abstract

This paper extends the multidimensional positive definite advection transport algorithm (MPDATA) to third-order accuracy for temporally and spatially varying flows. This is accomplished by identifying the leading truncation error of the standard second-order MPDATA, performing the Cauchy-Kowalevski procedure to express it in a spatial form and compensating its discrete representation—much in the same way as the standard MPDATA corrects the first-order accurate upwind scheme. The procedure of deriving the spatial form of the truncation error was automated using a computer algebra system. This enables various options in MPDATA to be included straightforwardly in the third-order scheme, thereby minimising the implementation effort in existing code bases. Following the spirit of MPDATA, the error is compensated using the upwind scheme resulting in a sign-preserving algorithm, and the entire scheme can be formulated using only two upwind passes. Established MPDATA enhancements, such as formulation in generalised curvilinear coordinates, the nonoscillatory option or the infinite-gauge variant, carry over to the fully third-order accurate scheme. A manufactured 3D analytic solution is used to verify the theoretical development and its numerical implementation, whereas global tracer-transport benchmarks demonstrate benefits for chemistry-transport models fundamental to air quality monitoring, forecasting and control. A series of explicitly-inviscid implicit large-eddy simulations of a convective boundary layer and explicitly-viscid simulations of a double shear layer illustrate advantages of the fully third-order-accurate MPDATA for fluid dynamics applications.

Keywords: Multidimensional advection, High-order schemes, Nonoscillatory schemes, Modified equation, Tracer transport

1. Introduction

Numerical modelling of advection in atmospheric flows is challenging. This is because of the highly variable multi-scale circulations and the need to respect the fundamental physical properties of transport, such as conservation, monotonicity, compatibility with mass continuity and correlations between tracers. Representations of moist processes or chemical reactions do not tolerate negative values, making sign preservation paramount. Balancing accuracy, efficiency and the physical realisability is problem specific and rarely straightforward. Consequently, there is a continuing quest for improved advection schemes applied in climate, weather and chemistry-transport models.

The key properties of a finite-difference approximation to any properly posed initial value problem are—in the spirit of the Lax's Equivalence Theorem—the consistency, stability and convergence (§3 in [1], §13.2 in [2]). The first two are necessary for the third that, per se, is a categorical imperative of computational physics. Inherent in the concept of convergence are the interrelated notions of the convergence rate and truncation error, epitomised by the order of accuracy. The latter is a simple single measure that reflects the dependence of the approximation's leading truncation error on the powers of the discretisation increments (spatial or temporal, or both) as well as the asymptotic rate at which the approximate solution converges

*Corresponding author
Email address: mwarusz@igf.fuw.edu.pl (Maciej Waruszewski)

to the sufficiently smooth genuine result in terms of the increments' powers as they tend to zero; cf. §7 in [1]. While high-order accuracy is a holy grail of numerical analysis, designing even a truly second-order method for practical problems of computational physics can be a difficult (if at all attainable) task; see [3], §20.5.2 in [2] and [4] for related discussions. Moreover, for complex computational models solving systems of inhomogeneous PDEs with multiplicity of the right-hand-side (rhs) forcings that act on disperse spatio-temporal scales, the asymptotic convergence rate may be practically inaccessible even though the employed method is formally sufficiently accurate. This, however, does not preclude the utility of high-order approximations, because the actual functional form of the leading truncation error can determine behavioural errors (such as excessive implicit diffusion or dispersion, lack of conservation or sign preservation, etc.), which for the application at hand can be more important than the formal accuracy (§III-A-23 in [5]).

Historically, the first-order-accurate advection schemes were discarded due to the notorious implicit diffusion, stimulating the development of second-order-accurate schemes. However, already in the seventies, higher-order schemes (i.e. third-order or higher) were shown to have computational advantages for atmospheric applications [6]. The key motivation is that higher-order accuracy can be more cost-effective than increasing resolution with a lower-order scheme, but there can be others related to the behavioural errors; e.g., a more uniform accuracy in terms of the Courant number and better preservation of the solution symmetries [7], or the strong stability at reduced dissipativity (see §5.4 in [1] for a substantive discussion). More recent studies demonstrated the efficiency of higher-order methods in the area of computational fluid dynamics [8] and in representing atmospheric wave motion [9], while a trend towards higher-order schemes can be observed for atmospheric models [10, 11, 12].

As it stands today, the term MPDATA encompasses a class of generally second-order accurate nonoscillatory forward-in-time advection algorithms, formulated as finite-difference (FD) schemes on structured rectilinear grids [13, 14] or finite-volume (FV) schemes on unstructured meshes [15, 16]. MPDATA schemes are based on iterative application of the first-order accurate upwind scheme, while exploiting its sign-preserving property [13]. In the first pass the transported variable is advected by the physical velocity, whereas subsequent passes use error-compensating pseudo-velocities designed to compensate the leading-order spatial and temporal truncation errors of the upwind scheme. Only one corrective pass is required for the second-order accuracy. MPDATA schemes have many virtues, including full multidimensionality, conservation, sign-preservation, nonlinear stability and relatively small phase error [14, 15]. Sign-preservation can be extended to monotonicity by means of the nonoscillatory option [17]. The nonoscillatory option is typically combined with the infinite-gauge (asymptotic limit of MPDATA for an infinite constant background), especially suitable for the transport of variable-sign fields and having favourable efficiency.

In order to guarantee the second-order accuracy in time the pseudo-velocities of MPDATA contain terms compensating the error of the forward-in-time differencing. This places MPDATA in a class of Lax-Wendroff schemes [18], that use the Cauchy-Kowalevski procedure [2] to transform temporal derivatives in the error terms into spatial derivatives while relying on the structure of the governing PDEs. Advantages of forward-in-time methods include the reduced storage requirements compared to multi-level schemes and the absence of computational modes such as those typical of basic centred-in-time schemes.

The Cauchy-Kowalevski procedure was also instrumental for transforming MPDATA into a family of solvers for generalised transport equations with arbitrary right-hand-sides in curvilinear coordinates [19, 14]. Simulations of high Reynolds number flows with the nonoscillatory MPDATA revealed the implicit large-eddy-simulation (ILES) property [20], subsequently studied in depth [21, 22, 23, 24, 25, 26] and verified in diverse geo- and astrophysical applications [27, 28, 29, 30, 31, 32].[1] Recent advances comprise soundproof-time-step semi-implicit integration schemes for the compressible Euler equations of all-scale atmospheric dynamics based on the FD [34] and the FV [16] MPDATA formulations. The FD-MPDATA is the basis of the EULAG model [28, 35] as well as an open-source free/libre solver library *libmpdata++*[2] [7], while

[1]The ILES property can be realised either through the action of the truncation terms of the basic MPDATA [22, 25], or via the nonoscillatory enhancement of the infinite-gauge option [20, 23, 24], or the basic MPDATA truncation combined with the nonoscillatory enhancement [27, 30, 31, 26, 33]. All three options have merits benefiting specialised applications.

[2]https://github.com/igfuw/libmpdataxx

the FV-MPDATA is employed in the Finite-Volume Module (FVM) for global all-scale atmospheric flows [36, 37].

Of particular relevance to the present work is reference [38], where a recursively summed error-compensating pseudo-velocity was derived and a third-order accurate FD-MPDATA was devised under the assumption of a constant physical velocity. To obtain the third-order accuracy two sources of error had to be compensated, the truncation error of the upwind scheme and the MPDATA corrective pass. The error was compensated by either using the recursive pseudo-velocity (resulting in a scheme with just one corrective iteration) or performing two corrective iterations. For problems where the velocity field changes in space or time, this variant of MPDATA is formally second-order accurate but, nonetheless, offers improved accuracy and diminishes the error dependence on the Courant number.

Here, we present an extension of the FD-MPDATA to the third-order accuracy for variable flows. In contrast with [38], we analytically derive the full truncation error of the second-order FD-MPDATA rather than solely the error of the first upwind pass. The error is then transformed into a spatial form following the Cauchy-Kowalevski procedure. This has the advantage that a two-pass third-order accurate scheme can be easily constructed, obviating the need for the recursive pseudo-velocity. For verifying the correctness of the analytic derivations as well as their numerical implementation, a manufactured 3D analytic solution is used, designed to have the full coordinate dependence of the advective velocity. To provide an example of intermediate complexity that is both relevant to atmospheric applications and facilitates comparisons to other advection algorithms popular in computational meteorology, two standard test cases for tracer transport in spatially variable time-dependent flows on the sphere are adopted. The first is the moving vortices on the sphere test case from [39]. The second is selected from the test suite in [40], and addresses tracer correlations in a reversing deformational flow. Having proved the newly developed advection scheme, we demonstrate its advantage to simulate fluid dynamics utilising two standard problems. Implicit large-eddy simulations of a convective boundary layer [20] address the scheme performance in highly turbulent natural flows, whereas a more academic problem of a viscous double shear layer rollup [41, 42] discriminately quantifies the benefit of the fully third-order MPDATA embedded in a lower-order accuracy flow solver.

The paper is organized as follows. In Section 2 we outline the standard FD-MPDATA scheme for the solution of a homogeneous generalised transport equation. Section 3 contains the novel truncation error analysis of the standard FD-MPDATA, presents the expression for the leading-order truncation error written as a pseudo-velocity, and discusses the origin of the terms that compose it. Section 4 constructs the fully third-order accurate MPDATA and provides details of its implementation. The proposed scheme is then verified and compared to the established MPDATAs in Section 5. Section 6 demonstrates the utility of the fully third-order-accurate MPDATA for simulation of fluid dynamics, and Section 7 concludes the paper.

2. Summary of the standard finite-difference MPDATA

We begin by reviewing the standard FD-MPDATA for integrating the homogeneous generalised transport equation

$$\frac{\partial G\Psi}{\partial t} + \nabla \cdot (\boldsymbol{V}\Psi) = 0 \, , \tag{1}$$

where $\Psi(t, \boldsymbol{x})$ is a nonnegative scalar field and $(t, \boldsymbol{x})$ are the independent curvilinear coordinates. The symbol $\nabla\cdot$ represents the scalar product of the nabla operator $\nabla = (\partial_x, \partial_y, \partial_z)$ with a vector. In general, the symbol G corresponds to the Jacobian of the coordinate transformation, the fluid density, or a product of both. Hereafter, we assume that it is independent of time $G = G(\boldsymbol{x})$. The vector field $\boldsymbol{V} = G\dot{\boldsymbol{x}}$ denotes a generalised flow field, where $\dot{\boldsymbol{x}}$ is the contravariant velocity in the underlying coordinate system.

A second-order accurate forward-in-time integral of (1) is written symbolically as

$$\Psi_{\boldsymbol{i}}^{n+1} = \Psi_{\boldsymbol{i}}^{n} - \frac{\delta t}{G_{\boldsymbol{i}}} \nabla \cdot \overline{(\boldsymbol{V}\Psi)}^{n+1/2} + \mathcal{O}(\delta t^3) \, , \tag{2}$$

where superscripts $n+1$ and n correspond, respectively, to the t^{n+1} and t^n time levels of a uniformly spaced temporal grid ($t^{n+1} = t^n + \delta t$ where δt is the time step) and cell centres of a rectilinear computational grid

$\boldsymbol{x_i}$ are labelled by the vector index $\boldsymbol{i} = (i, j, k)$ in 3D. The second term on the rhs of (2) represents the divergence of the advective flux at the intermediate time level $t^{n+1/2}$, and its discrete form defines a specific forward-in-time algorithm. MPDATA proceeds using the iterative form

$$\Psi_{\boldsymbol{i}}^{(m)} = \Psi_{\boldsymbol{i}}^{(m-1)} - \frac{1}{G_{\boldsymbol{i}}} \sum_{I=1}^{N} \left\{ F\left(\Psi_{\boldsymbol{i}}^{(m-1)}, \Psi_{\boldsymbol{i}+\boldsymbol{e}^I}^{(m-1)}, \mathcal{V}_{\boldsymbol{i}+1/2\,\boldsymbol{e}^I}^{I\ (m)}\right) - F\left(\Psi_{\boldsymbol{i}-\boldsymbol{e}^I}^{(m-1)}, \Psi_{\boldsymbol{i}}^{(m-1)}, \mathcal{V}_{\boldsymbol{i}-1/2\,\boldsymbol{e}^I}^{I\ (m)}\right) \right\} \tag{3}$$

for $m = 1, M$, where the parenthesised superscripts number the MPDATA iterations. The number of spatial dimensions is N, $\boldsymbol{e}^I$ denotes the unit vector with I indicating the coordinate direction, half integer indices correspond to cell faces and the upwind flux F is given as

$$F(\Psi_L, \Psi_R, \mathcal{V}) = 0.5\left[(|\mathcal{V}| + \mathcal{V})\Psi_L + (\mathcal{V} - |\mathcal{V}|)\Psi_R\right]. \tag{4}$$

At the start of the algorithm, $\Psi^{(0)} \equiv \Psi^n$, $\mathcal{V}^{I\ (1)} \equiv (\delta t/\delta x^I)(V^I)^{n+1/2}$, where δx^I is the grid spacing in the Ith coordinate direction. The Mth iteration of (3) yields the updated solution $\Psi^{n+1} \equiv \Psi^{(M)}$. Note that assumed here is the availability of an estimate for the local Courant number $\mathcal{V}^{I\,(1)}$ at the intermediate time level $t^{n+1/2}$ with at least $\mathcal{O}(\delta t^2)$ accuracy, discussed further in the paper. The second and subsequent iterations use the nondimensional error-compensating pseudo-velocities

$$\mathcal{V}^{I\ (m)} = \frac{\delta t}{\delta x^I} V^{I\,(m)} = \frac{\delta t}{\delta x^I} \overline{V}^I\left(\boldsymbol{V}^{(m-1)}, \Psi^{(m-1)}\right) \qquad \text{for } m > 1, \tag{5}$$

based on FD approximations to the analytical expression

$$\overline{\boldsymbol{V}}(\boldsymbol{V}, \Psi) = \frac{1}{2}\boldsymbol{\delta x} \odot \uparrow\!\boldsymbol{V}\!\uparrow \odot \frac{\nabla\Psi}{\Psi} - \frac{1}{2}\delta t \frac{\boldsymbol{V}}{G}\left[\boldsymbol{V} \cdot \frac{\nabla\Psi}{\Psi} + \nabla \cdot \boldsymbol{V}\right], \tag{6}$$

where $(\uparrow\!\boldsymbol{a}\!\uparrow)^I := |a^I|$ denotes component-wise absolute value of a vector and $(\boldsymbol{a} \odot \boldsymbol{b})^I := a^I b^I$ is the component-wise (Hadamard) product of two vectors. Reference [14] provides discrete expressions for (6), as well as a discussion of the consistency, stability and accuracy of the scheme.

3. Modified equation analysis of the standard MPDATA

This section presents the derivation of the leading order spatial and temporal truncation error of the standard MPDATA scheme. The temporal error is then expressed in a spatial form using the Cauchy-Kowalevski procedure. Hand derivations are supplemented with computer algebra results, that verify and extend the analysis. The spatial form of the error is presented as a pseudo-velocity, directly applicable to the construction of the fully third-order accurate MPDATA. The origin of the various error components is then discussed.

3.1. Hand derivation

The essence of the modified equation analysis of the standard MPDATA can be summarised in three conceptually distinct steps. First, every $\Psi_{\boldsymbol{i}}^{(m-1)}$, $\mathcal{V}_{\boldsymbol{i}+1/2\,\boldsymbol{e}^I}^{I\ (m)}$ and $G_{\boldsymbol{i}}$ that appears in (3) is expanded in a Taylor series in space about a common point $\mathbf{x_i}$. The second step involves the third-order Taylor series expansion in time of the spatial expansion result about t^n. The resulting modified equation is of the form

$$\frac{\partial\Psi}{\partial t} + \frac{1}{G}\nabla \cdot (\boldsymbol{V}\Psi) = \frac{1}{G}\nabla \cdot (\boldsymbol{T}_F) - \frac{\delta t}{2}\frac{\partial^2\Psi}{\partial t^2} - \frac{\delta t^2}{6}\frac{\partial^3\Psi}{\partial t^3} + \mathcal{O}^3(\delta t, \boldsymbol{\delta x}), \tag{7}$$

where $\boldsymbol{T}_F$ symbolises the truncation error of the MPDATA fluxes. Hereafter, $\mathcal{O}^r(\delta t, \boldsymbol{\delta x})$ refers to any terms of order greater or equal to r when considered as a polynomial in the variables δt and $\boldsymbol{\delta x}$. The final step involves applying the Cauchy-Kowalevski procedure to (7), i.e. successively using (7) and its time derivatives to express the truncation error solely in terms of spatial derivatives of the transported scalar. Importantly, for the third-order accuracy, using (7) as opposed to (1) to perform the conversion is essential [43, 38]. The end result can be expressed as follows

$$\frac{\partial \Psi}{\partial t} + \frac{1}{G}\nabla \cdot (\boldsymbol{V}\Psi) = \frac{1}{G}\nabla \cdot (\boldsymbol{T}_S) := \frac{1}{G}\nabla \cdot \left(\overline{\overline{\boldsymbol{V}}}\Psi\right), \tag{8}$$

where the $\mathcal{O}^3(\delta t, \boldsymbol{\delta x})$ terms were dropped, $\boldsymbol{T}_S$ symbolises the spatial form of the truncation error, and the last equality defines $\overline{\overline{\boldsymbol{V}}}$—the third-order error-compensating velocity. Following the outlined approach, the detailed derivation of the truncation error of the standard MPDATA with two iterations is presented in Appendix A. A unified expression for $\overline{\overline{\boldsymbol{V}}}$, combining the computer algebra extensions presented in the subsequent Section 3.2, is shown and discussed in Section 3.3.

3.2. Computer algebra implementation

While the procedure presented in the previous subsection is fairly straightforward, the analytical manipulations can become involving, especially when extensions, such as going beyond two iterations, are considered. To validate and extend the modified equation analysis of MPDATA, the computer algebra system SageMath[3] was used to implement the procedure. The implementation uses computer algebra capabilities judiciously to keep the truncation error in the divergence form. The approach is briefly summarised below.

Notwithstanding the iterative nature of MPDATA, the scheme can be formally written as

$$\Psi_{\boldsymbol{i}}^{n+1} = \Psi_{\boldsymbol{i}}^{n} - \frac{1}{G_{\boldsymbol{i}}}\sum_{I=1}^{N}\left[F^{I\ [MP]}_{\boldsymbol{i}+1/2\boldsymbol{e}^I} - F^{I\ [MP]}_{\boldsymbol{i}-1/2\boldsymbol{e}^I}\right], \tag{9}$$

where $\boldsymbol{F}^{[MP]}$ is the MPDATA numerical flux, i.e. the sum over all iterations in (3). Formally expanding (9) to third-order accuracy in time and space leads to (7) with

$$\boldsymbol{T}_F = -\frac{\boldsymbol{\delta x}}{\delta t} \odot \left(\boldsymbol{F}^{[MP]} + \frac{\boldsymbol{\delta x}\odot\boldsymbol{\delta x}}{24}\odot\nabla\odot\nabla\odot\boldsymbol{F}^{[MP]}\right) + \boldsymbol{V}\Psi. \tag{10}$$

Writing $\frac{\partial^2\Psi}{\partial t^2}$ and $\frac{\partial^3\Psi}{\partial t^3}$ on the rhs of (7) as $\frac{\partial}{\partial t}\left(\frac{\partial\Psi}{\partial t}\right)$ and $\frac{\partial^2}{\partial t^2}\left(\frac{\partial\Psi}{\partial t}\right)$, respectively, and using $\frac{\partial\Psi}{\partial t}$ based on (7) in the resulting expression gives

$$\frac{\partial \Psi}{\partial t} + \frac{1}{G}\nabla \cdot (\boldsymbol{V}\Psi) = \frac{1}{G}\nabla \cdot \left[\boldsymbol{T}_F - \frac{\delta t}{2}\frac{\partial}{\partial t}\left(\boldsymbol{T}_F - \boldsymbol{V}\Psi\right) + \frac{\delta t^2}{12}\frac{\partial^2}{\partial t^2}\left(\boldsymbol{T}_F - \boldsymbol{V}\Psi\right)\right] + \mathcal{O}^3(\delta t, \boldsymbol{\delta x}). \tag{11}$$

Equation (11) is the starting point for the automated Cauchy-Kowalevski procedure, which is only applied to the terms under the divergence operator on the rhs of (11), thus keeping the result in the divergence form.

3.3. Third-order error-compensating velocity

The explicit expression for the third-order error-compensating velocity $\overline{\overline{\boldsymbol{V}}}$ is

$$\begin{aligned}\overline{\overline{\boldsymbol{V}}}(\boldsymbol{V}, \overline{\boldsymbol{V}}, \Psi) = & \underbrace{-\frac{\boldsymbol{\delta x}\odot\boldsymbol{\delta x}}{24}\odot\left[4\boldsymbol{V}\odot\frac{1}{\Psi}\nabla\odot\nabla\Psi + 2\frac{\nabla\Psi}{\Psi}\odot\nabla\odot\boldsymbol{V} + \alpha\nabla\odot\nabla\odot\boldsymbol{V}\right]}_{A} \\ & + \underbrace{\beta_M\frac{\boldsymbol{\delta x}}{2}\odot\uparrow\overline{\boldsymbol{V}}\uparrow\odot\frac{\nabla\Psi}{\Psi}}_{B} + \underbrace{\frac{\delta t}{2}\boldsymbol{\delta x}\odot\uparrow\boldsymbol{V}\uparrow\odot\frac{1}{\Psi}\nabla\left[\frac{1}{G}\nabla\cdot(\boldsymbol{V}\Psi)\right]}_{C} \\ & \underbrace{-\frac{\delta t^2}{3}\frac{\boldsymbol{V}}{G\Psi}\nabla\cdot\left[\frac{\boldsymbol{V}}{G}\nabla\cdot(\boldsymbol{V}\Psi)\right]}_{D} + \underbrace{\frac{\delta t^2}{24}\left[\gamma\frac{\partial^2\boldsymbol{V}}{\partial t^2} + \frac{2\boldsymbol{V}}{G\Psi}\nabla\cdot\left(\frac{\partial\boldsymbol{V}}{\partial t}\Psi\right) - \frac{2}{G\Psi}\frac{\partial\boldsymbol{V}}{\partial t}\nabla\cdot(\boldsymbol{V}\Psi)\right]}_{E},\end{aligned} \tag{12}$$

[3] https://www.sagemath.org/

where α, β_M and γ are parameters that result from different MPDATA formulations.

Each term on the rhs of (12) originates from a source of third-order error in the basic algorithm and has a clear interpretation, for the subsequent discussion they are labelled with letters A to E. The first two terms A and B both originate from upwind differencing, A corresponds to the third-order error of the first upwind pass, while B is related to the upwinding based on the pseudo-velocity in the second pass. Noteworthy, the term B is $\mathcal{O}^2(\delta t, \boldsymbol{\delta x})$ as $\overline{\boldsymbol{V}}$ is composed of terms proportional to $\boldsymbol{\delta x}$ and δt. The term C is a result of the iterative nature of MPDATA, specifically it comes from using the first-order accurate upwind solution in calculating gradients of Ψ that enter the pseudo-velocity formula (6). The last two terms D and E are both related to the forward-in-time differencing errors. The terms differ in that D derives only from the temporal variations of Ψ, whereas E includes contributions from the time-varying velocity field. In the case of stationary flow the term E vanishes identically.

The parameters α, β_M and γ on the rhs of (12) combine three different MPDATA formulations into a common formula. Within the limits of the third-order accurate analysis, the only effect of increasing the number of MPDATA passes beyond two is the cancellation of the B term. Consequently, β_M is equal to one if $M = 2$ and zero otherwise. In flow solvers the velocity is often interpolated to the cell faces using $V^I_{\boldsymbol{i}+1/2\boldsymbol{e}^I} = \frac{1}{2}(V^I_{\boldsymbol{i}} + V^I_{\boldsymbol{i}+\boldsymbol{e}^I})$. This interpolation procedure introduces another source of a third-order error. In principle a higher-order interpolation could be used, however, it is usually more convenient to account for this error directly in the third-order error-compensating velocity. The parameter α is equal to 4 when the standard interpolation procedure is used, and 1 if $V^I_{\boldsymbol{i}+1/2\boldsymbol{e}^I}$ is known to $\mathcal{O}(\boldsymbol{\delta x}^3)$. Similarly, the second-order MPDATA requires an estimate of $V^{n+1/2}$ with $\mathcal{O}(\delta t^2)$ accuracy. In soundproof models, the most common procedure is linear extrapolation $\boldsymbol{V}^{n+1/2} = \frac{1}{2}(3\boldsymbol{V}^n - \boldsymbol{V}^{n-1})$[4] which maintains mass continuity. The error of this estimate can also be directly incorporated into the third-order error-compensating velocity by choosing $\gamma = 10$. Otherwise, if $\boldsymbol{V}^{n+1/2}$ is at least $\mathcal{O}(\delta t^3)$ accurate, $\gamma = 1$. The meaning and values of α, β_M and γ are collected in Table 1.

Table 1
Summary of various options in MPDATA and the corresponding values of the parameters α, β_M and γ appearing in (12).

Condition	Parameter	Value
$V^I_{\boldsymbol{i}+1/2\boldsymbol{e}^I}$ is at least $\mathcal{O}(\boldsymbol{\delta x}^3)$ accurate	α	1
$V^I_{\boldsymbol{i}+1/2\boldsymbol{e}^I} = \frac{1}{2}(V^I_{\boldsymbol{i}} + V^I_{\boldsymbol{i}+\boldsymbol{e}^I})$	α	4
$M = 2$	β_M	1
$M > 2$	β_M	0
$\boldsymbol{V}^{n+1/2}$ is at least $\mathcal{O}(\delta t^3)$ accurate	γ	1
$\boldsymbol{V}^{n+1/2} = \frac{1}{2}(3\boldsymbol{V}^n - \boldsymbol{V}^{n-1})$	γ	10

4. Construction and implementation of the fully third-order accurate MPDATA

Here, we construct a third-order accurate MPDATA based on the expression for the third-order error-compensating velocity. As in the standard MPDATA, the general idea is to subtract an estimate of the third-order error by using $\overline{\overline{\boldsymbol{V}}}$ in an upwind iteration. In the simplest way, it can be done in just two iterations of the form (3), by replacing the nondimensional pseudo-velocity in the second iteration (5) with

[4]The given formula assumes, in accordance with the derivation in the text, a uniform time step. See [44] for variable time stepping that also accounts for time-dependent curvilinear coordinates.

the sum of the standard MPDATA pseudo-velocity and the third-order error-compensating pseudo-velocity

$$\mathcal{V}^{I\ (2)} = \frac{\delta t}{\delta x^I}\left[\overline{V}^I\left(\boldsymbol{V}^{(1)},\Psi^{(1)}\right) + \overline{\overline{V}}^I\left(\boldsymbol{V}^{(1)},\overline{\boldsymbol{V}}(\boldsymbol{V}^{(1)},\Psi^{(1)}),\Psi^{(1)}\right)\right]. \tag{13}$$

Performing only two iterations is computationally efficient and can benefit parallel distributed-memory communication. However, it is worth pointing out other possibilities, potentially admitting larger time steps δt,[5] such as first proceeding with all of the standard MPDATA iterations and then applying an extra upwind pass based solely on $\overline{\overline{\boldsymbol{V}}}$.

The discrete formulation of $\overline{\overline{\boldsymbol{V}}}$ completes the definition of the fully third-order accurate scheme. Following the decomposition in (12), we write $\overline{\overline{V}}^I_{\boldsymbol{i}+1/2\boldsymbol{e}^I} = A_d + B_d + C_d + D_d + E_d$, where

$$\begin{aligned}A_d =& -\frac{1}{3}V^I_{\boldsymbol{i}+1/2\boldsymbol{e}^I}\frac{|\Psi_{\boldsymbol{i}+2\boldsymbol{e}^I}| - |\Psi_{\boldsymbol{i}+\boldsymbol{e}^I}| - |\Psi_{\boldsymbol{i}}| + |\Psi_{\boldsymbol{i}-\boldsymbol{e}^I}|}{|\Psi_{\boldsymbol{i}+2\boldsymbol{e}^I}| + |\Psi_{\boldsymbol{i}+\boldsymbol{e}^I}| + |\Psi_{\boldsymbol{i}}| + |\Psi_{\boldsymbol{i}-\boldsymbol{e}^I}| + \epsilon} \\ &- \frac{1}{12}\left(V^I_{\boldsymbol{i}+3/2\boldsymbol{e}^I} - V^I_{\boldsymbol{i}-1/2\boldsymbol{e}^I}\right)\frac{|\Psi_{\boldsymbol{i}+\boldsymbol{e}^I}| - |\Psi_{\boldsymbol{i}}|}{|\Psi_{\boldsymbol{i}+\boldsymbol{e}^I}| + |\Psi_{\boldsymbol{i}}| + \epsilon} - \frac{\alpha}{24}\left(V^I_{\boldsymbol{i}+3/2\boldsymbol{e}^I} + V^I_{\boldsymbol{i}-1/2\boldsymbol{e}^I} - 2V^I_{\boldsymbol{i}+1/2\boldsymbol{e}^I}\right),\end{aligned} \tag{14}$$

$$B_d = \beta_M|\overline{V}^I_{\boldsymbol{i}+1/2\boldsymbol{e}^I}|\frac{|\Psi_{\boldsymbol{i}+\boldsymbol{e}^I}| - |\Psi_{\boldsymbol{i}}|}{|\Psi_{\boldsymbol{i}+\boldsymbol{e}^I}| + |\Psi_{\boldsymbol{i}}| + \epsilon}, \tag{15}$$

$$C_d = \frac{\delta t}{2}\frac{|V^I_{\boldsymbol{i}+1/2\boldsymbol{e}^I}|}{\langle|\Psi|\rangle_C + \epsilon}\left\{\frac{[\nabla\cdot(\boldsymbol{V}|\Psi|)]_{\boldsymbol{i}+\boldsymbol{e}^I}}{G_{\boldsymbol{i}+\boldsymbol{e}^I}} - \frac{[\nabla\cdot(\boldsymbol{V}|\Psi|)]_{\boldsymbol{i}}}{G_{\boldsymbol{i}}}\right\}, \tag{16}$$

$$D_d = -\frac{\delta t^2}{3}\frac{V^I_{\boldsymbol{i}+1/2\boldsymbol{e}^I}}{G_{\boldsymbol{i}+1/2\boldsymbol{e}^I}(\langle|\Psi|\rangle_D + \epsilon)}\sum_{J=1}^{N}\frac{1}{\delta x^J}\left\{\frac{[\nabla\cdot(\boldsymbol{V}|\Psi|)]_{\boldsymbol{i}+1/2\boldsymbol{e}^I+1/2\boldsymbol{e}^J}}{G_{\boldsymbol{i}+1/2\boldsymbol{e}^I+1/2\boldsymbol{e}^J}} - \frac{[\nabla\cdot(\boldsymbol{V}|\Psi|)]_{\boldsymbol{i}+1/2\boldsymbol{e}^I-1/2\boldsymbol{e}^J}}{G_{\boldsymbol{i}+1/2\boldsymbol{e}^I-1/2\boldsymbol{e}^J}}\right\}, \tag{17}$$

$$\begin{aligned}E_d =& \frac{\delta t^2\gamma}{24}\left(\frac{\partial^2 V^I}{\partial t^2}\right)_{\boldsymbol{i}+1/2\boldsymbol{e}^I} + \frac{\delta t^2 V^I_{\boldsymbol{i}+1/2\boldsymbol{e}^I}}{12G_{\boldsymbol{i}+1/2\boldsymbol{e}^I}(\langle|\Psi|\rangle_E + \epsilon)}\left[\nabla\cdot\left(\frac{\partial\boldsymbol{V}}{\partial t}|\Psi|\right)\right]_{\boldsymbol{i}+1/2\boldsymbol{e}^I} \\ &- \frac{\delta t^2}{12G_{\boldsymbol{i}+1/2\boldsymbol{e}^I}(\langle|\Psi|\rangle_E + \epsilon)}\left(\frac{\partial V^I}{\partial t}\right)_{\boldsymbol{i}+1/2\boldsymbol{e}^I}[\nabla\cdot(\boldsymbol{V}|\Psi|)]_{\boldsymbol{i}+1/2\boldsymbol{e}^I}.\end{aligned} \tag{18}$$

Like in all previous MPDATA formulations, normalisation of the truncation error expressions with $\sim\Psi$ is performed in a way that ensures boundedness of the error-compensating pseudo-velocities, and thus the stability of the scheme [14, 15, 16]. Specifically, we construct the normalisation as an average over all discrete Ψ's that enter the discretisation of the term that this factor is multiplying. This is written explicitly in (14)-(15), and symbolically as $\langle|\Psi|\rangle_C$, $\langle|\Psi|\rangle_D$ and $\langle|\Psi|\rangle_E$ in (16)-(18). Note that in (14)-(18), every Ψ has been replaced with the corresponding absolute value $|\Psi|$ which extends the scheme for transport of fields with variable sign [14]. Standardly for MPDATA [13], an arbitrary small constant ϵ—e.g. 10^{-15} in 64-bit precision for fields with the amplitude of $\mathcal{O}(1)$—is added in the normalisations in (14)-(18) to ensure the validity of the scheme when $\langle|\Psi|\rangle_{\dots} = 0$.[6]

[5] Implementations summing pseudo-velocities of corrective iterations generally have more restrictive Courant-number condition sufficient for the linear stability; see §5.5 in [13] and §6.1 in [38] for discussions.

[6] Implementations with $\epsilon \equiv 0$ are possible but less cost-effective.

The divergence of a product of an arbitrary vector field $\boldsymbol{\omega}$ with a scalar field ϕ is formulated as

$$[\nabla \cdot (\boldsymbol{\omega}\phi)]_{\boldsymbol{i}} = \sum_{I=1}^{N} \frac{1}{\delta x^I} \left(\omega^I_{\boldsymbol{i}+1/2\boldsymbol{e}^I} \phi_{\boldsymbol{i}+1/2\boldsymbol{e}^I} - \omega^I_{\boldsymbol{i}-1/2\boldsymbol{e}^I} \phi_{\boldsymbol{i}-1/2\boldsymbol{e}^I} \right). \tag{19}$$

Whenever the values of scalar or vector fields are needed at points where they are not located, a suitable average based on the minimal number of points is used, for example $\phi_{\boldsymbol{i}+1/2\boldsymbol{e}^I} = \frac{1}{2}(\phi_{\boldsymbol{i}+\boldsymbol{e}^I} + \phi_{\boldsymbol{i}})$ for a scalar field and $\boldsymbol{\omega}_{\boldsymbol{i}} = \frac{1}{2}(\boldsymbol{\omega}_{\boldsymbol{i}+1/2\boldsymbol{e}^I} + \boldsymbol{\omega}_{\boldsymbol{i}-1/2\boldsymbol{e}^I})$ for a vector field. Especially in the context of fluid solvers, the expressions for the first and second time derivative of velocity in (18) have to be known only to $\mathcal{O}(\delta t)$ in order to ensure the third-order accuracy of the scheme. Consequently, simple backward differentiation formulae can be used to obtain them.

The enhancements to the standard MPDATA algorithm discussed in the introduction, such as the nonoscillatory option and the infinite-gauge, carry over to the proposed scheme. Technically, the infinite-gauge variant is achieved by replacing in the second MPDATA iteration the first two arguments of the upwind flux function with unity, substituting every $|\Psi|$ that enters the denominators of the third-order error-compensating velocity (14)-(18) with unity as well as the remaining $|\Psi|$ with Ψ, multiplying the pseudo-velocity terms independent of Ψ by $\Psi_{\boldsymbol{i}+1/2\boldsymbol{e}^I}$ and setting the value of the parameter $\beta_M = 0$—see e.g. [16] for the altered discrete formulae with the second-order FV-MPDATA.

5. Results of numerical advection tests

5.1. Preamble

Herein we verify the newly developed fully third-order accurate MPDATA and assess its merits compared to the established variants of the scheme. We consider three test problems, solely in the context of the homogeneous transport equation (1), for which sufficiently smooth genuine solutions are known, at least in selected time instants, thereby enabling rigorous accuracy analysis. The first test problem uses a bespoke 3D solution with a stationary Jacobian and a non-stationary generalised flow field, manufactured [45] to verify the correctness of the theoretical development and its numerical implementation. The remaining two problems employ established benchmarks [39, 40], designed to typify difficulties encountered in a long range tracer advection at the heart of atmospheric chemistry-transport models—of the utmost importance to monitoring, forecasting and controlling air pollution across scales from micrometeorology to climate; see [46, 47, 48, 49, 50, 51] for a sample of representative works that address relevant computational issues over the three decades. Both benchmarks idealise two-dimensional tracer transport on the sphere in rotating deformational flows. The first benchmark addresses a cross-polar transport in a velocity field composed of two vortices advected over the poles; whereas, the second focuses on tracer correlations in a reversible deformational flow that leads to tracer filamentation and its reversal—the latter phase being important to source detection of, e.g., nuclear testing [52].

In all three advection tests the fully third-order accurate scheme is compared with MPDATA using the constant-velocity third-order correction from [38]. For tracer transport on the sphere results using the nonoscillatory infinite-gauge variant of second-order accurate MPDATA are provided as a reference. In those examples, the nonoscillatory infinite-gauge variant of the fully third-order accurate scheme is also examined to see how well the new advancement combines with the previous developments. Table 2 lists all the schemes used in the paper. The numerical solution error was measured in the standard ℓ_2 norm

$$\ell_2 = \sqrt{\frac{\sum_{\boldsymbol{i}} G_{\boldsymbol{i}}(\Psi_{\boldsymbol{i}} - \Psi^e_{\boldsymbol{i}})^2}{\sum_{\boldsymbol{i}} G_{\boldsymbol{i}}(\Psi^e_{\boldsymbol{i}})^2}} \tag{20}$$

where $\Psi^e_{\boldsymbol{i}}$ is the exact solution evaluated at the point $\boldsymbol{x}_{\boldsymbol{i}}$.

As every test considered here uses a prescribed time-dependent flow field, the velocities at the intermediate time level $t^{n+1/2}$ were calculated directly from the analytical expressions. For the manufactured solution and the reversing deformational flow the velocities were evaluated directly at the cell faces, whereas in the moving vortices test the velocity was first calculated at the grid points and then interpolated (cf. the second row of Table 1). Similarly, the time derivatives of velocity, needed in (18), were calculated based on the analytical formulae for the manufactured solution and the reversing deformational flow but based on second-order centred finite-differences for the moving vortices.

Table 2
Summary and labels of the various MPDATA formulations utilised in the simulations of §5 and §6.

Label	Scheme
Mp2	fully second-order-accurate MPDATA
Mp3	fully third-order-accurate MPDATA
Mp3cc	third-order constant-coefficient MPDATA
Mg2No	nonoscillatory infinite-gauge variant of second-order-accurate MPDATA
Mg3No	nonoscillatory infinite-gauge variant of Mp3
Mg3ccNo	nonoscillatory infinite-gauge variant of Mp3cc

5.2. Manufactured solution in 3D

Using the method of manufactured solutions [45] the following analytical solution of the transport equation (1) was constructed

$$\Psi(t, \boldsymbol{x}) = (2 + \sin t \sin x)(2 + \sin t \sin y)(2 + \sin t \sin z) \ , \tag{21}$$

with the corresponding coefficients

$$G(\boldsymbol{x}) = e^{\cos x + \cos y + \cos z} \ , \tag{22}$$

$$V^I(t, \boldsymbol{x}) = \frac{G \cos t}{2 + \sin t \sin x^I} \ . \tag{23}$$

The solution Ψ can be interpreted as a fluid density that obeys the continuity equation formulated in curvilinear coordinates with the Jacobian G. Note that the flow field contains regions of strong convergence and divergence (the ratio of the divergence reciprocal to the advective time scale is ~ 0.1 near the divergence extrema), consequently the uniform initial condition $\Psi(0, \boldsymbol{x}) = 8$ gets shaped into a sinusoidal pattern.

The generalised transport equation (1) was solved in a triply periodic domain $[0, 2\pi] \times [0, 2\pi] \times [0, 2\pi]$ discretised on a $N \times N \times N$ regular Cartesian grid. For the convergence study a range of values $N = 9, 17, 33, 65, 129$ was chosen. The time step was continuously adapted such that the maximum Courant number did not exceed 0.5. The solution error was calculated at the final time $t = 1$, chosen to prevent the possibility of error cancellations due to the flow symmetries.

Two sets of simulations were performed, one using the proposed fully third-order accurate MPDATA (Mp3), and second using the established MPDATA that is third-order accurate for constant flows (Mp3cc). Convergence of the error measure under the grid refinement is shown on Figure 1. Results confirm the third-order convergence of the Mp3 scheme, while the convergence of the Mp3cc scheme reduces to second-order due to the variability of the flow.

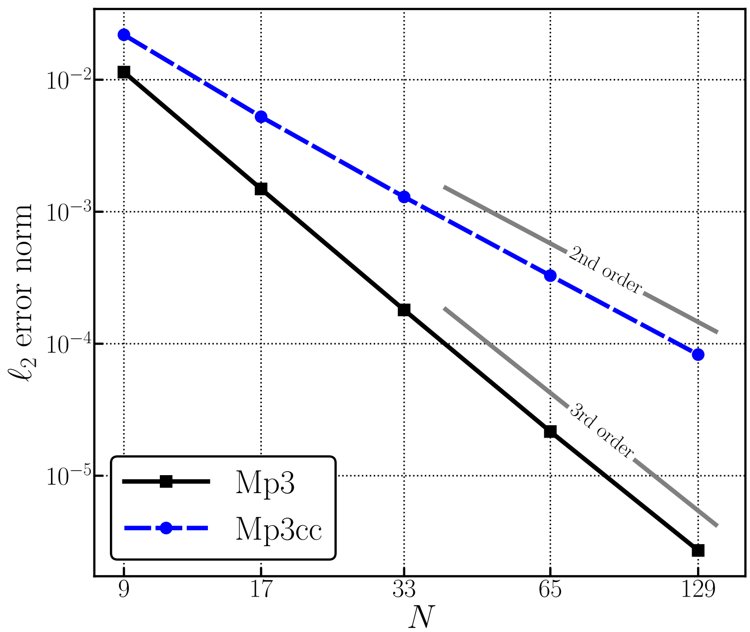

Fig. 1. Numerical convergence to the manufactured solution in the ℓ_2 error norm at time $t = 1$.

5.3. Moving vortices

To assess the accuracy of the fully third-order accurate scheme for tracer transport on the sphere a two-dimensional test case was adopted from [39]. It specifies an initial distribution of a tracer field together with a non-divergent, variable in time and space, deformational flow field such that the analytical solution of (1) at any given moment is readily available. The flow field is composed of two vortices, which are always located on the opposite sides of the sphere and embedded in a background solid-body rotation. Here, the rotation angle of the background flow was set to $\pi/2$, corresponding to the cross-polar flow. All other parameters of the test case were set following the numerical experiments in [39]. Initially, the centre of one of the vortices was located at $(3\pi/2, 0)$ in longitude-latitude coordinates. Consequently, the initial position of the second vortex was $(\pi/2, 0)$. One full rotation of the vortices over the poles takes 12 days. Figure 2a and Figure 2b depict the initial condition of the tracer field and its exact distribution after 12 days, respectively.

The numerical solution was computed on a regular longitude-latitude grid with $(2N+1)\times N$ points, corresponding to uniform $\delta\lambda = \delta\theta = \pi/N$ grid increments. Simulations were run with $N = 24, 48, 96, 192, 384, 768$. Differencing in the vicinity of the poles follows the principles of differential geometry applied to the longitude-latitude coordinate system, see [53] for a discussion. As in the preceding example the time step was continuously adapted to keep the maximum Courant number less than a prescribed value, here equal to 1. The simulation time of 12 days corresponds to one full rotation of the vortices over the poles. Here, selected schemes of Table 2 are compared. Two of them are the same as in the preceding example—the novel Mp3 scheme and the established Mp3cc scheme. Moreover, the Mg3No scheme combines the novel third-order infinite-gauge with the nonoscillatory option. Simulations using the standard nonoscillatory infinite-gauge MPDATA (Mg2No) serve as a reference to evaluate accuracy of the third-order schemes.

Convergence in the ℓ_2 error measure with increasing resolution is shown in Figure 3. In the range of simulated N the proposed Mp3 scheme converges the fastest at a rate slightly higher than third. In contrast, the Mp3cc scheme does not sustain a third-order rate and reduces to second-order convergence. Enforcing monotonicity in the third-order accurate Mg3No leads to a significant loss of accuracy and basically second-order convergence. The reference Mg2No shows the largest errors and second-order convergence achieved only over the finest grids. Even though three of the four schemes end up converging at a second-order rate, there are marked differences between their accuracy. On the finest grid $N = 768$, the ℓ_2 error norms span almost two orders of magnitude between the various schemes.

Table 3 lists runtimes of the MPDATA schemes relative to the upwind scheme, based on the $N = 192$ simulations. In addition, the sign-preserving second-order accurate MPDATA scheme (Mp2) is also included for reference. The relative runtimes for Mp2 and Mp3 are ~ 3.6 and ~ 10.3, respectively, i.e. roughly a cost factor of ~ 3 to increase the order by one (up to three). The relative runtimes for the two monotone MPDATA schemes are ~ 5.9 and ~ 12.6, showing the significantly smaller cost increase when going from second- to third-order than first- to second-order. Importantly, the fully third-order accurate Mp3 scheme is only slightly more expensive than the constant-coefficients variant Mp3cc.

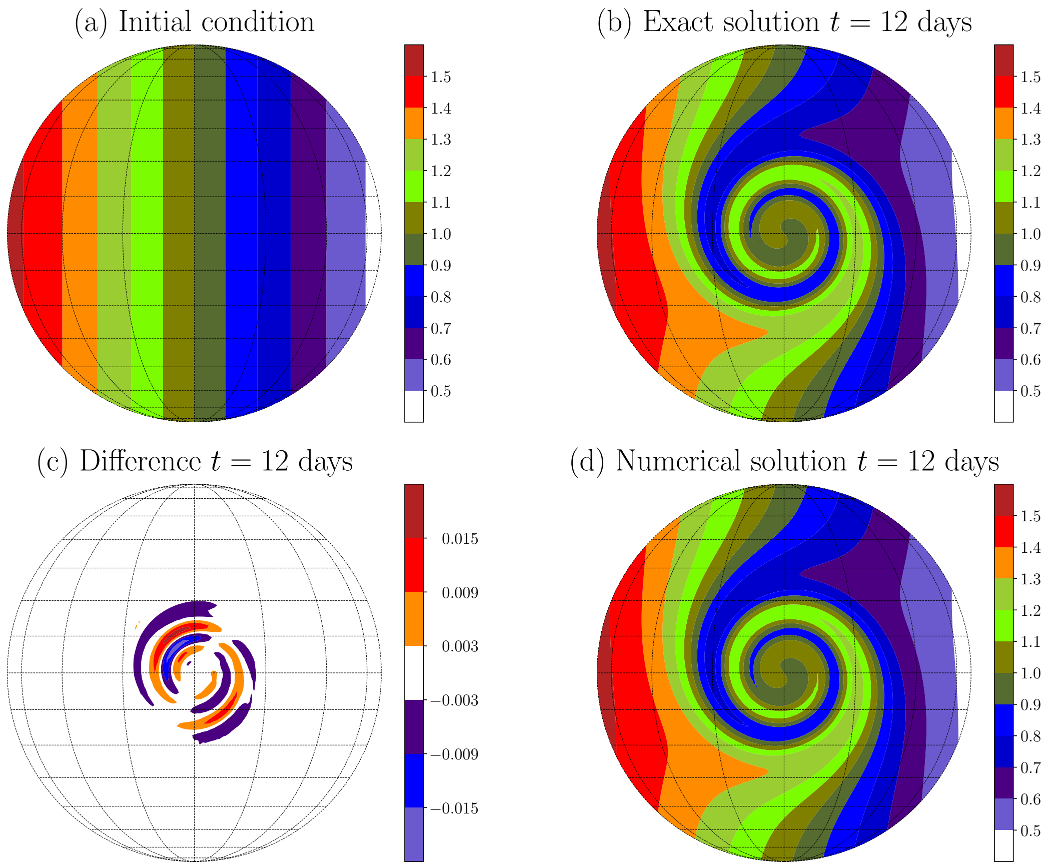

Fig. 2. The initial condition (a) together with the analytical solution (b), the difference between the numerical and the analytical solution (c) and the numerical solution (d) after one rotation of the vortices over the poles for the moving vortices test case. The numerical solution was obtained using the Mp3 scheme on a grid with $N = 192$, see subsection 5.3 for details.

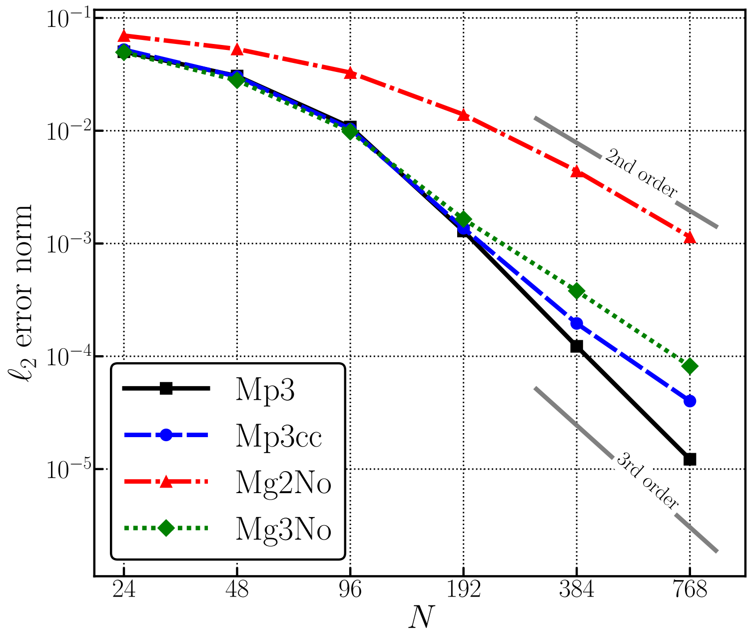

Fig. 3. Numerical convergence in the ℓ_2 error norm for the moving vortices test case. The error was evaluated after one rotation of the vortices over the poles.

Table 3
Runtimes of the MPDATA schemes relative to the upwind scheme, based on the moving vortices test case. See subsection 5.3 for details.

Upwind	Mp2	Mg2No	Mp3cc	Mp3	Mg3No
1.0	3.6	5.9	9.5	10.3	12.6

5.4. Reversing deformational flow

In [40], the authors introduced a test suite for a two-dimensional transport on the sphere using various prescribed time-dependent deformational flow fields. Results of the test suite for a variety of state-of-the-art schemes were collected in [54]. Here, we evaluate selected diagnostics from this test suite for the schemes tested in §5.3.

The setup specifies four different initial conditions for the tracer field, each composed of two distributions in the same shape centred at $(\pi/2, 0)$ and $(3\pi/2, 0)$, respectively. The four different shapes are Gaussian hill, cosine bell, slotted cylinder and 'correlated' cosine bell. Two wind fields, one non-divergent and one divergent, were prescribed in the test suite. Here, we consider only diagnostics based on the non-divergent wind field. As in the previous example, the flow field is composed of a deformational part and the solid-body rotation part. The solid-body rotation is purely in the zonal direction. Contrary to the previous example, the deformational part of the flow has a temporal dependence that leads to the flow reversal halfway through the rotation. Hence, after the full rotation, the initial conditions should be recovered. For the detailed specification of the setup in terms of analytical formulae the reader is referred to [40].

As in the preceding example, we used a regular longitude-latitude grid with $(2N + 1) \times N$ points. Simulations were performed with $N = 60, 120, 240, 480, 960$ corresponding to $\delta\lambda = \delta\theta$ between 3° and 0.1875°. Again, a variable time step was employed with the maximum Courant number kept just under 0.8. The total time of each simulation corresponded to one full rotation.

Figure 4 shows the numerical solution for each initial condition, midway through the simulation, obtained with the Mg3No scheme using a $\delta\lambda = 1.5°$ grid interval. No oscillations can be seen, even for the discontinuous slotted cylinders initial conditions (Figure 4c). More quantitatively, normalised deviations from the initial extrema $(\min \Psi^n - \min \Psi^0)/\max \Psi^0 = 0$ and $(\max \Psi^n - \max \Psi^0)/\max \Psi^0 = -0.001$ for the slotted cylinders at the time of the maximal deformation. This shows the effective combination of the developed third-order scheme with the nonoscillatory option of MPDATA. Overall, the filamentary structure of the solutions at the time of the maximal deformation seems to be well captured.

The first quantitative metric is the convergence in the ℓ_2 error norm with the increasing resolution using the Gaussian hill initial condition, presented on Figure 5. In a stark difference to the preceding example, the results obtained using the Mp3, Mp3cc and Mg3No schemes are nearly identical. Each of the aforementioned schemes converges at the third-order with negligible differences in the error norm. The lack of improvement in accuracy with the fully third-order accurate scheme can be attributed to the compact $\mathcal{C}^\infty$ support of the initial conditions that leads to the filamentary structure of the solution during most of the simulation time. Consequently, there is a scale separation between the smooth large-scale flow variations and the sharper gradients of the transported tracer. The truncation error associated with the flow variability is therefore much smaller than the error due to the tracer gradients, the latter of which is fully compensated to third-order by both the Mp3cc and Mp3 schemes. This hypothesis was tested by repeating the convergence test using the initial condition of the previous example in the considered flow field, resulting in the Mp3 scheme converging at the third order and the Mp3cc scheme falling off the third-order convergence line. Without cross-polar transport, the nonoscillatory scheme Mg3No retains the third-order convergence due to the MPDATA nonscillatory option blending first- and higher-order schemes with consistently low phase errors [17].

Motivated by transport of long-lived species in the stratosphere or aerosol-cloud interactions, the authors in [40] included a set of diagnostics that assess the ability of a scheme to preserve "pre-existing" functional relations. The setup involves the cosine bell initial conditions and another initial condition constructed from it, dubbed 'correlated' cosine bells. The construction is based on applying pointwise the non-linear functional relation $\xi(\chi) = -0.9\chi^2 + 0.8$ where χ is the value of the cosine bells tracer. Ideally, this relation should be preserved during the simulation, the correlation plot of ξ and χ plotted at the time of the maximal deformation shows the degree of numerical numerical mixing introduced by the scheme. Furthermore, the numerical mixing can be classified into mixing resembling real mixing in the atmosphere, "range-preserving" unmixing and overshooting, which are quantified by the corresponding ℓ_r, ℓ_u and ℓ_o measures [55].

Figure 6 presents the correlation plot and the numerical mixing measures for the four schemes considered in this example, computed on the grid with the $\delta\lambda = 0.75°$ intervals. The Mp3 scheme shows less of both the "real" mixing and the unmixing compared to the Mp3cc scheme. As both schemes are only sign-preserving they show some degree of overshooting, similar in magnitude. The overshooting is entirely eliminated by the nonoscillatory Mg2No and Mg3No schemes, that also exhibit smaller values of "real" mixing. Both "real" mixing and "range-preserving" unmixing diagnostics are better for the Mg3No scheme featuring the full third-order corrections. The measure of unmixing is similar with the Mp3 scheme and its nonoscillatory infinite-gauge counterpart Mg3No. The results presented here can be compared to the results obtained using a variety of state-of-the-art schemes in [54], section 3.5 therein. For example, values for the shape-preserving versions of the MPAS and the CAM-FV advection schemes at $\delta\lambda = 0.75°$, which can be directly compared to Mp3No, are $(l_r, l_u, l_o) = (6.43 \times 10^{-4}, 3.06 \times 10^{-4}, 0)$ and $(l_r, l_u, l_o) = (3.11 \times 10^{-4}, 1.98 \times 10^{-4}, 6.86 \times 10^{-5})$.

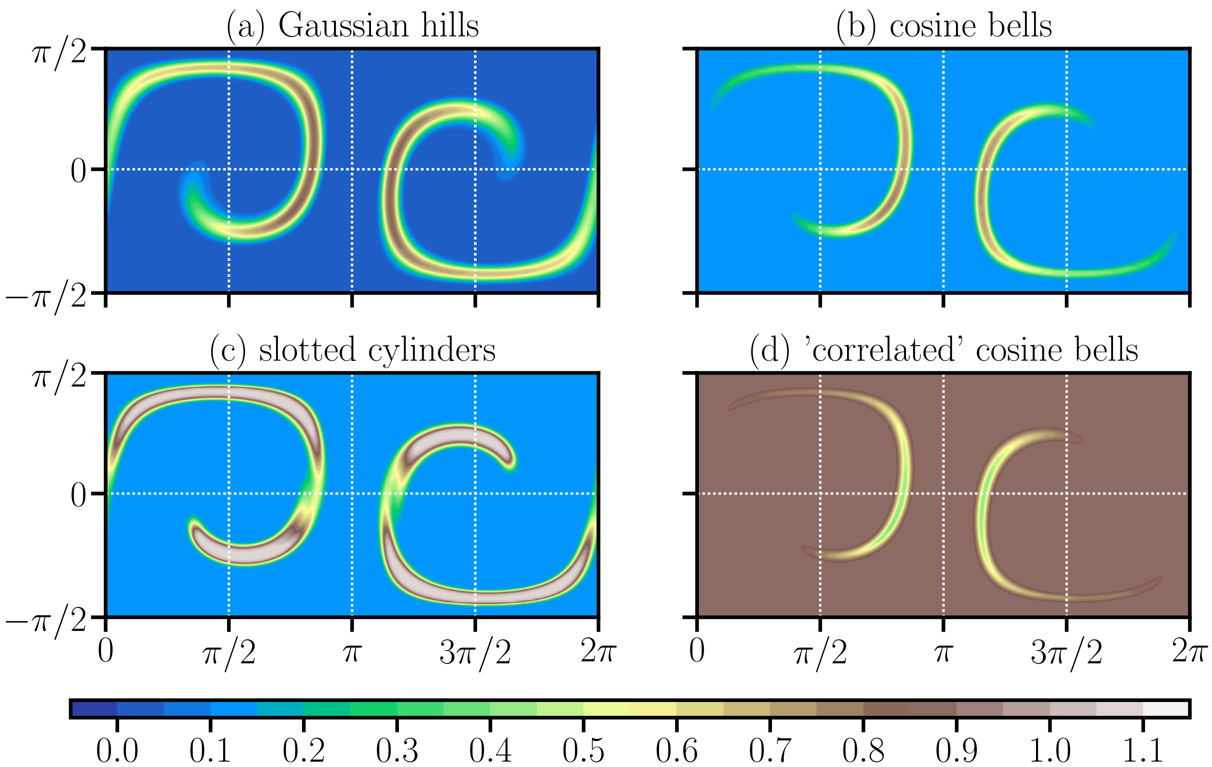

Fig. 4. Tracer fields for the reversing deformational flow at the time of the maximal deformation. The results were obtained using the Mg3No scheme on a grid with $N = 120$ ($\delta\lambda = 1.5°$), see subsection 5.4 for details.

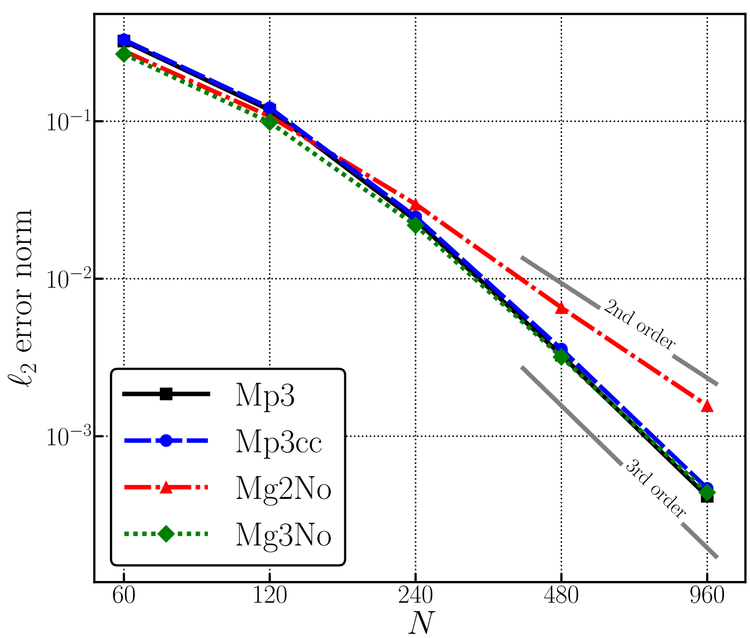

Fig. 5. Numerical convergence for the Gaussian hills initial condition of the reversing deformational flow test in the ℓ_2 error norm. The error was evaluated when the tracer first returned to its initial position.

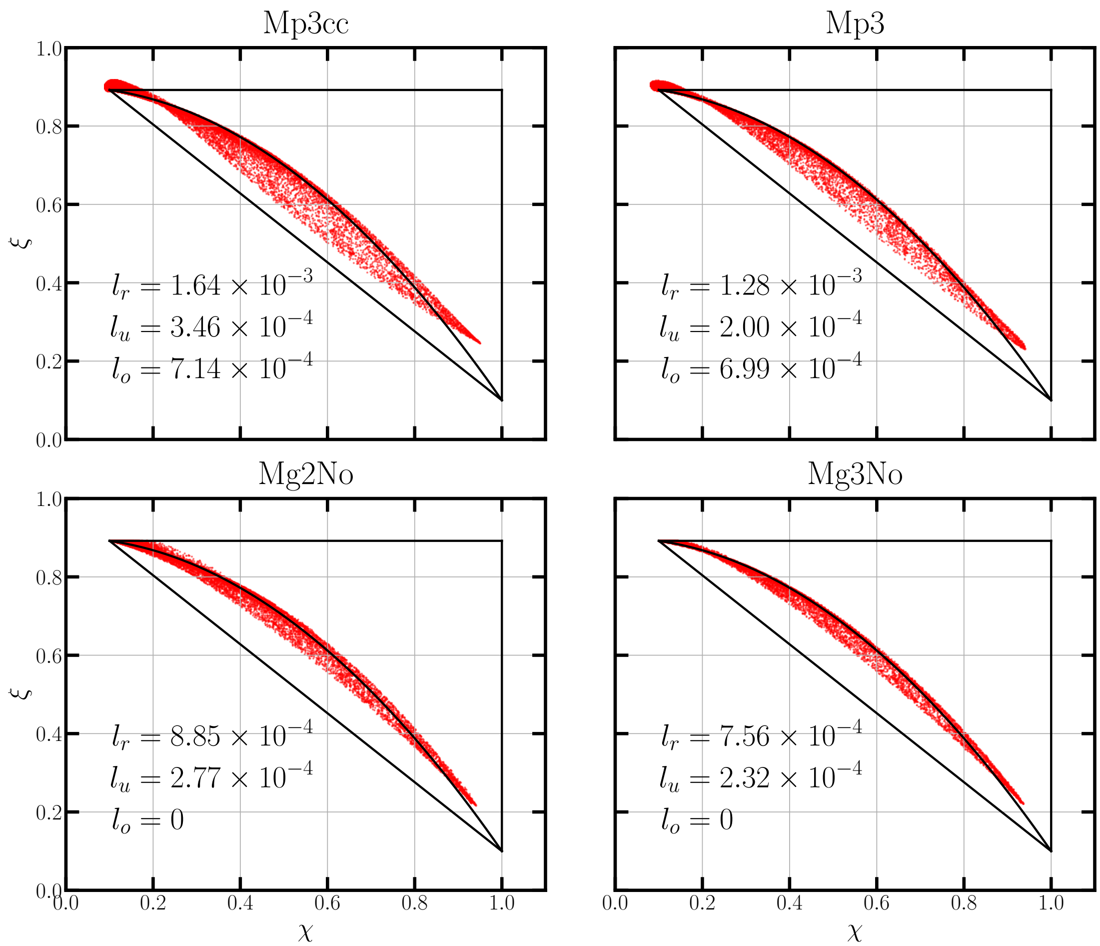

Fig. 6. Scatter plots showing preservation of the pre-existing functional relation for the reversing deformational flow test. The results for the 'correlated' cosine bells (ξ) versus cosine bells (χ) are shown at the time of the maximal deformation on a grid with $N = 240$ ($\delta\lambda = 0.75°$). The solid lines indicate the regions used to classify the numerical mixing. The mixing diagnostics ℓ_r, ℓ_u, ℓ_o are given for each scheme. See subsection 5.4 for details.

6. Fluid dynamics applications

6.1. *MPDATA based integrator for an archetype fluid problem*

To substantiate the significance of the new development beyond the passive tracer advection, we start with a synopsis of the MPDATA-based flow solvers, widely documented in the literature [28, 35, 34, 36].

In simulation of fluid dynamics, the prognostic governing PDEs can be viewed as a system of nonlinear inhomogeneous transport equations

$$\frac{\partial G\Psi}{\partial t} + \nabla \cdot (\boldsymbol{V}\Psi) = GR, \tag{24}$$

with the rhs forcings GR generally dependent on all prognostic variables. Given a fully second-order accurate forward-in-time advection algorithm (2) for the homogeneous transport problem (1), written in short as

$$\Psi_{\boldsymbol{i}}^{n+1} = \mathcal{A}_{\boldsymbol{i}}(\Psi^n, \mathbf{V}^{n+1/2}, G) \ , \tag{25}$$

the inhomogeneous problem (24) is integrated to the second-order accuracy with the template algorithm

$$\Psi_{\boldsymbol{i}}^{n+1} = \mathcal{A}_{\boldsymbol{i}}(\Psi^n + 0.5\delta t R^n, \mathbf{V}^{n+1/2}, G) + 0.5\delta t R_{\boldsymbol{i}}^{n+1} \ , \tag{26}$$

provided at least $\mathcal{O}(\delta t^2)$ estimates of the advective velocity $\mathbf{V}^{n+1/2}$ and the rhs forcing R^{n+1} [19, 56, 34]. Advecting half of the rhs' trapezoidal integral effectively adds to the solution the term $-\delta t G^{-1}\nabla\cdot(0.5\delta t \mathbf{V} R)$ that compensates, to the second-order accuracy, the first-order truncation error term revealed by the Cauchy-Kowalevski procedure employed in derivation of the MPDATA integrator for the inhomogeneous transport problem [19]. Assuring fully third-order-accurate solutions to a complete system of fluid equations requires accounting for such coupling terms as well as fully third-order-accurate representation of the rhs. This may be virtually impossible in a paradigm of essentially two-time-level integrators. Moreover, the requirements such as the solution monotonicity [17], compatibility of scalar conservation laws with their Lagrangian forms [44, 36, 37], or compatibility of elliptic Poisson/Helmholtz operators with advection [34] may take precedence over the formal accuracy, for the sake of physical realisability and efficacy in complex simulations. Nevertheless, the increased accuracy of the homogeneous algorithm $\mathcal{A}_{\boldsymbol{i}}$ can benefit the overall accuracy of integrations, as evidenced by the subsequent examples.

In the following §6.2 and §6.3, all simulations use the nonoscillatory infinite-gauge variants of, respectively, the second-order accurate (Mg2No), the third-order constant coefficient (Mg3ccNo) and the fully third-order accurate (Mg3No) MPDATA. Advective velocities were linearly extrapolated to the intermediate time level and interpolated to cell faces.

6.2. ILES of convective boundary layer

The small-scale, inherently nonhydrostatic problem of turbulent convective boundary layer [20] standardly assumes the incompressible Boussinesq limit of the all-scale Euler equations [34]. Assuming a quiescent environment with background potential temperature $\Theta(z)$ such that $\Theta(z=0)=\Theta_o=$ const., and density $\rho(z)=\rho_o=$ const., the governing Boussinesq PDEs in a Cartesian reference frame are compactly written as

$$\begin{aligned} &\frac{\partial \mathbf{u}}{\partial t} + \nabla\cdot(\mathbf{u}\otimes\mathbf{u}) = -\nabla\varphi - \mathbf{g}\frac{\theta}{\Theta_o} + \boldsymbol{\mathcal{D}}(\mathbf{u},\theta)\ , \\ &\frac{\partial \theta}{\partial t} + \nabla\cdot(\mathbf{u}\theta) = -\mathbf{u}\cdot\nabla\Theta + \mathcal{H}\ , \\ &\nabla\cdot\mathbf{u} = 0\ . \end{aligned} \tag{27}$$

Here, $\mathbf{u}=(u^1,u^2,u^3)$ and θ denote velocity vector and potential temperature perturbation with respect to the ambient state, φ is the density normalised pressure perturbation and $\mathbf{g}=(0,0,-g)$ marks the gravitational acceleration; whereas the terms $\boldsymbol{\mathcal{D}}$ and $\mathcal{H}$ refer to dissipative and diabatic forcings in the momentum and entropy equations, respectively. The equations of the system (27) are of the form (24)—with $G\equiv\rho_o$, Ψ corresponding to θ and components of $\mathbf{u}$, and R representing the associated rhs—whereby integrations of (27) adopt the template algorithm (26).[7]

Figure 7 highlights the explicitly-inviscid ILES solutions generated with nonoscillatory infinite-gauge options of the second-order-accurate, third-order-accurate for constant coefficients and fully third-order accurate MPDATA. As the accuracy of the advection scheme increases, the power spectra and profiles evince, respectively, increasing length of the inertial range and amplification of the variance. This is consistent with increasing effective resolution of the simulation—cf. Figs. 6-8 in [57]—or, alternatively, the effective Reynolds number; see §6.5.7 in [58]. Furthermore, Fig. 8 shows the instantaneous vertical-velocity field organized into characteristic Rayleigh-Bénard cells [29] evincing improved regularity for the full third-order accuracy, as opposed to the constant-coefficient case of the MPDATA advection. Nonetheless both are superior to the Mg2No solution, whose representative example can be seen in Fig. 3 of reference [59] after which we adopted the model setup.[8] The latter result indicates that the implicit subgrid-scale model contained in the trunca-

[7] Completing the solution to (27) requires combining templates (26) for θ and vertical velocity component u^3 into the closed form expression for $\mathbf{u}|^{n+1}$, subsequently plugged into the discrete form of the mass continuity equation of (27) to generate the elliptic boundary value problem for φ [34, 36]; for compatibility of θ advection with the elliptic solver, $\alpha\equiv 0$ in (14).

[8] In brief, the horizontally periodic domain $3200\times3200\times1500$ m^3 is resolved with $65\times65\times51$ regular grid over 15000 s ($\sim$ 13 large eddy-turnover times) with $\delta t=8$ s. The ambient $\Theta(z)=300$ K up to 500 m and $\Theta(z)=\Theta_o[1+Sz]$ aloft with the stratification $S=10^{-5}$ m^{-1}; surface heat flux $H_o=0.01$ Kms^{-1}, and our convective scales $z_i=690.0$ m, $w^*=0.613$ ms^{-1}, $t^*=1126.2$ s and $T^*=0.0163$ K closely match those in the first row of Table 1 in [59].

tion terms of the Mg3No scheme may be even more scale selective than in second-order MPDATAs [23, 26]; cf. §3.3 in [60] for a discussion. Notwithstanding the improvements in the solution quality with the increasing accuracy of the MPDATA advection, all three results are formally at most second-order-accurate.

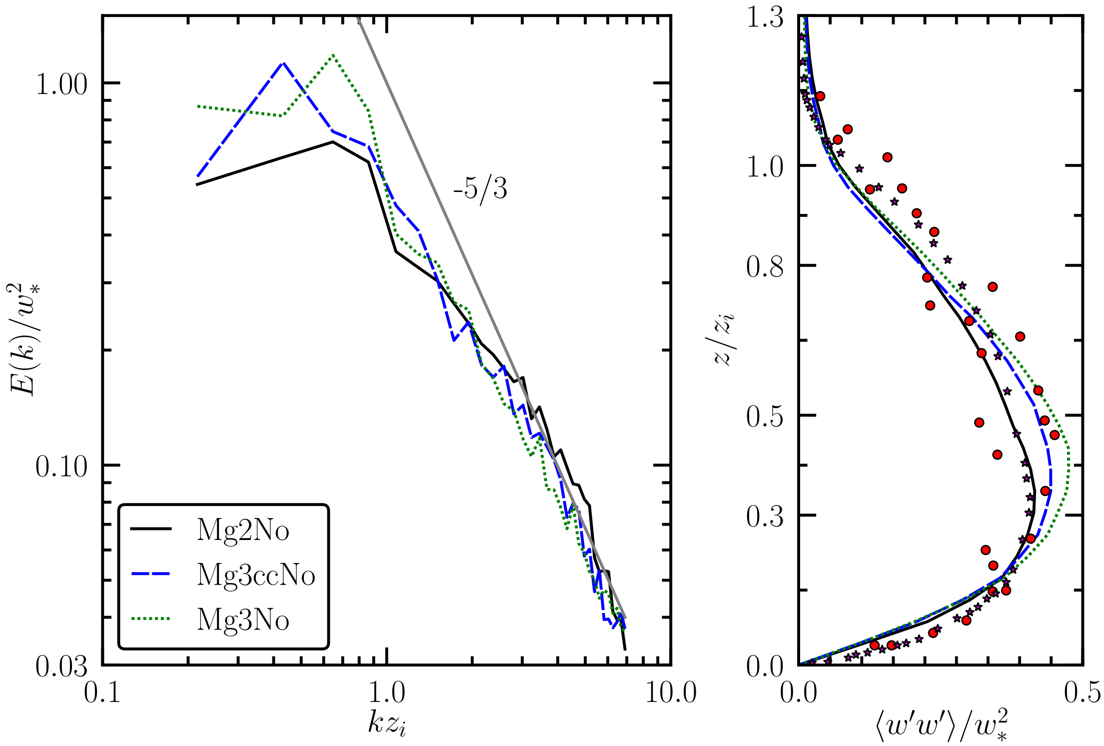

Fig. 7. Normalised instantaneous (at $t/t^* \approx 13$ large eddy-turnover times) vertical velocity spectra (at $z/z_i = 0.4$) and variance profiles in ILES simulations of the convective boundary layer, employing Mg2No, Mg3ccNo and Mg3No advection; stars denote the explicit LES result of [60] generated with second-order-accurate centred-in-space differencing, and red circles represent field and laboratory data.

6.3. Viscous rollup of a double shear layer

Following Brown and Minion [61, 62], the rollup of a double shear layer has become an accuracy benchmark for assessing the performance of various of numerical methods designed to integrate incompressible Navier-Stokes equations—a special case of (27) with identically vanishing g, θ and $\mathcal{H}$. The charm of the problem is its relative simplicity,[9] together with the discriminating accuracy indicator of producing (or not) at coarse resolutions superfluous eddies compared to the pristine converged result with two eddies [41, 42]. With this respect, Fig. 9 is self-evident showing for the same grid the increased accuracy of the solutions based on the fully third-order-accurate advection solver.

[9]The dimensionless problem is posed on a 2D doubly-periodic Cartesian domain of a unit linear extent, with the divergence free initial condition $u^1 = \tanh((y-0.25)\delta)$ if $y \leq 0.5$ and $u^1 = \tanh((0.75-y)\delta)$ otherwise, and $u^2 = v' sin(2\pi x)$; the parameter δ (here $\delta = 100$) controls the thickness of the shear layer, a small perturbation $v' = 0.05$, and constant viscosity $\nu = 0.5 \cdot 10^{-4}$ so the Reynolds number $Re = 10^4$.

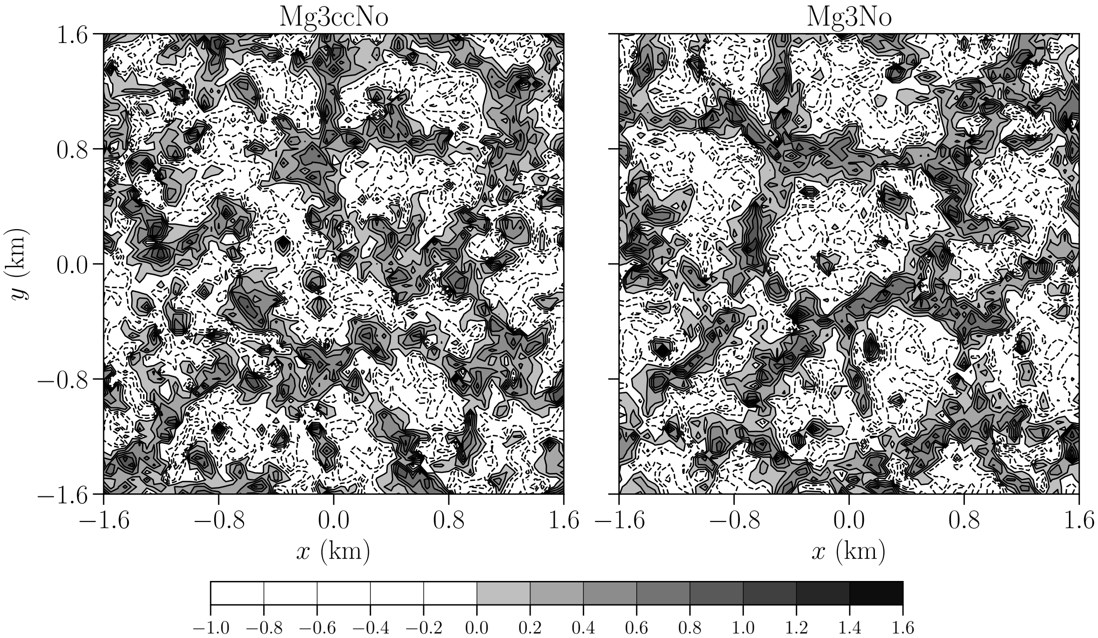

Fig. 8. Vertical velocity field u^3 [ms^{-1}] in the $x-y$ plane at $z/z_i \approx 0.2$ and $t/t^* \approx 13$, using Mg3ccNo and Mg3No advection.

Table 4
Error norm ℓ_2 of u^1 velocity component for the double shear layer example calculated at $t = 1.5$. Reference solution was obtained on a 2049×2049 grid with Mg3No.

Grid	Mg2No	Order	Mg3ccNo	Order	Mg3No	Order
129×129	3.35×10^{-1}	—	3.65×10^{-1}	—	5.96×10^{-2}	—
257×257	1.96×10^{-1}	0.77	1.09×10^{-1}	1.74	4.83×10^{-2}	0.30
513×513	7.21×10^{-2}	1.44	2.90×10^{-2}	1.91	1.57×10^{-2}	1.62
1025×1025	2.05×10^{-2}	1.82	7.06×10^{-3}	2.04	4.29×10^{-3}	1.87

Table 4 quantifies the accuracy of the selected MPDATA options and corroborates the discussion of the preceding subsection. While for each resolution the Mg3No scheme is consistently the most accurate, the convergence rate of all schemes appears to approach the second-order asymptotic limit; however this is not formally ensured as the diffusion terms are integrated only to $\mathcal{O}(\delta t^2)$. The quickest accuracy gain of the Mg3ccNo result is correlated with its largest error at the coarse resolution where the solution is topologically inconsistent with the converged result.

7. Conclusion

A fully third-order accurate MPDATA advection scheme under a temporally and spatially varying flow has been developed. The foundation of the proposed scheme lies in the rigorous modified equation analysis of the standard MPDATA, followed by expressing the spatial form of the error as the divergence of an advective flux. The discrete error estimate is compensated in the subsequent upwind pass, resulting in a third-order-accurate sign-preserving scheme. The scheme requires only two upwind passes, which can benefit parallel distributed-memory communication.

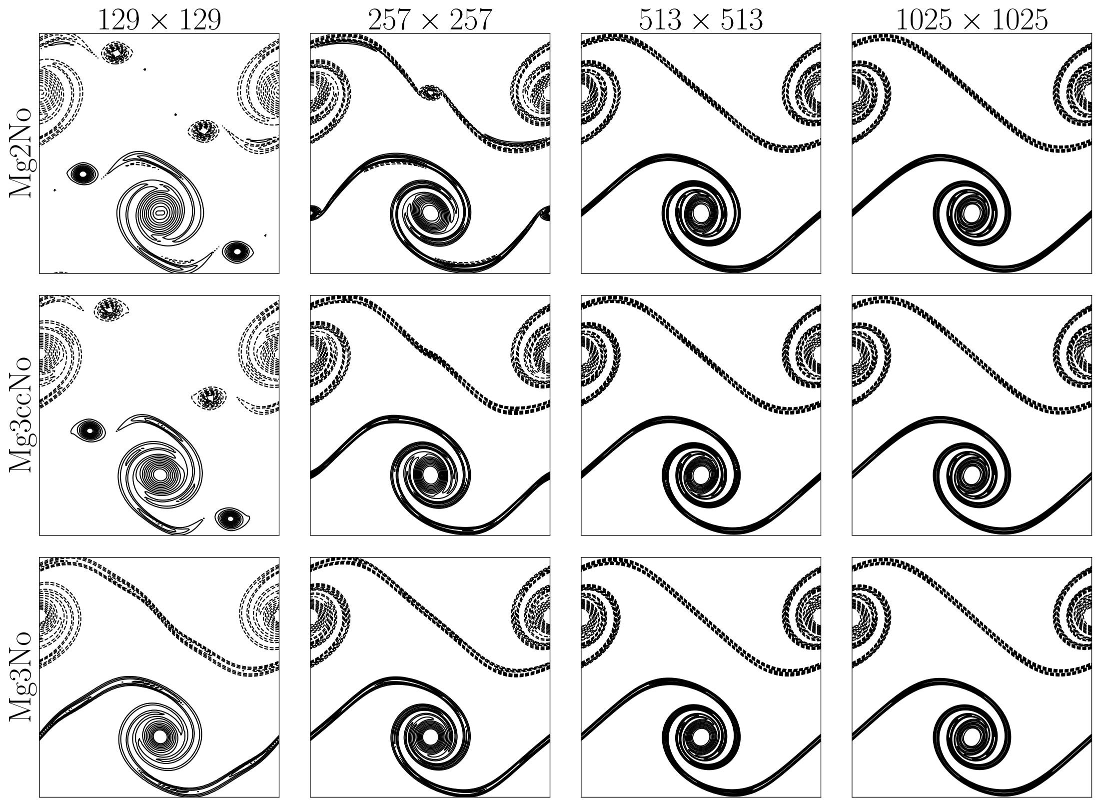

Fig. 9. Vorticity isolines for Mg2No, Mg3ccNo and Mg3No advection (top to bottom) for 129×129, 257×257, 513×513 and 1025×1025 doubly periodic grids (left to right).

The main building block of the proposed scheme is the third-order error-compensating pseudo-velocity, which was derived in a continuous form and later discretised on a structured rectilinear computational grid. To provide insight into the various sources of the standard MPDATA error, the pseudo-velocity was separated into select terms with a clear interpretation. Using a computer algebra system, the third-order error-compensating velocity was augmented with terms that compensate errors of common interpolation and extrapolation procedures in implementations of the standard MPDATA.

Three-dimensional numerical convergence tests based on a manufactured solution verified the third-order accuracy of the scheme. Two benchmarks of tracer advection in time-varying rotating deformational flows on the sphere—pertinent to global chemistry-transport models—were used to compare the proposed scheme with the established MPDATA formulations. The novel third-order accurate MPDATA showed a robust decrease in the solution error compared to the established third-order constant-coefficient scheme. Moreover, the fully third-order scheme with nonoscillatory enhancement is substantially more accurate than the established nonoscillatory MPDATAs. The novel scheme can also much better preserve functional correlations between the tracers. Evaluation of the computational cost showed the efficacy of the fully third-order accurate MPDATA schemes, with about the same cost as the third-order constant-coefficient scheme.

Simulations of complete fluid equations for the evolution of a convective boundary layer and the rollup of a double shear layer provide numerical solutions that are at most second-order accurate, yet still reveal overall accuracy gains and advantageous ILES properties of the advective transport based on the fully third-order-accurate scheme. Because the latter option comes at about the same computational expense as its constant-coefficients predecessor, it is a valuable addition to the MPDATA based fluid-dynamics codes. An increased complexity of the new scheme is offset by the general accessibility of its source code. The developments presented in this paper are available as part of the open-source *libmpdata++* library [7]. The source code that reproduces the results and plots presented in Section 5 is freely available at the project repository[10], while the computer algebra scripts used in Section 3 are provided separately [11].

Acknowledgements

Helpful comments from two anonymous referees are gratefully acknowledged. MW and HP acknowledge support from Poland's National Science Centre (Narodowe Centrum Nauki) [decision no. 2012/06/M/ST10/00434 (HARMONIA)]. This work was supported in part by funding received from the European Research Council under the European Union's Seventh Framework Programme (FP7/2012/ERC Grant agreement no. 320375)

Appendix A. Detailed modified equation analysis of the standard MPDATA with two iterations

A.1. Expansion in space

By expanding the first iteration of MPDATA, $m = 1$ in (3), in Taylor series about a common spatial point $\boldsymbol{x_i}$ and omitting its index we obtain

$$\Psi^{(1)} = \Psi^n + \frac{\delta t}{G}\nabla\cdot\left\{-\boldsymbol{V}^{n+1/2}\Psi^n + \frac{\boldsymbol{\delta x}}{2}\odot\left\uparrow\boldsymbol{V}^{n+1/2}\right\uparrow\odot\nabla\Psi^n + \boldsymbol{H}_{UPW}\right\} + O^4(\delta t, \boldsymbol{\delta x}), \tag{A.1}$$

$$\boldsymbol{H}_{UPW} = -\frac{\boldsymbol{\delta x}\odot\boldsymbol{\delta x}}{24}\odot\left(4\boldsymbol{V}^{n+1/2}\odot\nabla\odot\nabla\Psi^n + 2\nabla\Psi^n\odot\nabla\odot\boldsymbol{V}^{n+1/2} + \Psi^n\nabla\odot\nabla\odot\boldsymbol{V}^{n+1/2}\right). \tag{A.2}$$

Similarly, for the second iteration, $m = 2$ in (3), under the assumption that the discrete approximations to the pseudo-velocity components at the staggered spatial grid points are at least second-order accurate, leads to

$$\Psi^{n+1} = \Psi^{(1)} + \frac{\delta t}{G}\nabla\cdot\left\{-\overline{\boldsymbol{V}}^{n+1/2,\,(1)}\Psi^{(1)} + \frac{\boldsymbol{\delta x}}{2}\odot\left\uparrow\overline{\boldsymbol{V}}^{n+1/2,\,(1)}\right\uparrow\odot\nabla\Psi^{(1)}\right\} + O^4(\delta t, \boldsymbol{\delta x}), \tag{A.3}$$

where a shorthand notation $\overline{\boldsymbol{V}}^{a,\,b} = \overline{\boldsymbol{V}}(\boldsymbol{V}^a, \Psi^b)$ was adopted.

By using the definition of pseudo-velocity (6) in the first term under the divergence operator on the rhs of (A.3) we are left with

$$\begin{aligned}\Psi^{n+1} = \Psi^{(1)} + \frac{\delta t}{G}\nabla\cdot\Bigg\{ &-\frac{\boldsymbol{\delta x}}{2}\odot\left\uparrow\boldsymbol{V}^{n+1/2}\right\uparrow\odot\nabla\Psi^{(1)} + \frac{\delta t}{2G}\boldsymbol{V}^{n+1/2}\nabla\cdot\left(\boldsymbol{V}^{n+1/2}\Psi^{(1)}\right) \\ &+\frac{\boldsymbol{\delta x}}{2}\odot\left\uparrow\overline{\boldsymbol{V}}^{n+1/2,\,(1)}\right\uparrow\odot\nabla\Psi^{(1)}\Bigg\} + O^4(\delta t, \boldsymbol{\delta x}).\end{aligned} \tag{A.4}$$

In order to eliminate $\Psi^{(1)}$ from (A.4) we proceed in two steps. First, we use (A.1) in the first term on the rhs of (A.4) which results in

$$\begin{aligned}\Psi^{n+1} = \Psi^n + \frac{\delta t}{G}\nabla\cdot\Bigg\{ &-\boldsymbol{V}^{n+1/2}\Psi^n - \frac{\boldsymbol{\delta x}}{2}\odot\left\uparrow\boldsymbol{V}^{n+1/2}\right\uparrow\odot\left(\nabla\Psi^{(1)} - \nabla\Psi^n\right) \\ +\frac{\delta t}{2G}\boldsymbol{V}^{n+1/2}\nabla\cdot\left(\boldsymbol{V}^{n+1/2}\Psi^{(1)}\right) &+ \frac{\boldsymbol{\delta x}}{2}\odot\left\uparrow\overline{\boldsymbol{V}}^{n+1/2,\,(1)}\right\uparrow\odot\nabla\Psi^{(1)} + \boldsymbol{H}_{UPW}\Bigg\} + O^4(\delta t, \boldsymbol{\delta x}).\end{aligned} \tag{A.5}$$

[10] https://github.com/igfuw/libmpdataxx/tree/master/tests/mp3_paper_2018_JCP
[11] https://github.com/igfuw/mpdata_mea

As (A.1) implies

$$\nabla\Psi^{(1)} = \nabla\Psi^n - \delta t \nabla\left[\frac{1}{G}\nabla\cdot\left(\boldsymbol{V}^{n+1/2}\Psi^n\right)\right] + O^2(\delta t, \boldsymbol{\delta x}) \ , \tag{A.6}$$

$$\nabla\cdot\left(\boldsymbol{V}^{n+1/2}\Psi^{(1)}\right) = \nabla\cdot\left(\boldsymbol{V}^{n+1/2}\Psi^n\right) - \delta t\nabla\cdot\left[\frac{\boldsymbol{V}^{n+1/2}}{G}\nabla\cdot\left(\boldsymbol{V}^{n+1/2}\Psi^n\right)\right] + O^2(\delta t, \boldsymbol{\delta x}) \ , \tag{A.7}$$

we apply (A.1), (A.6) and (A.7) to the rhs of (A.5) with the result being

$$\Psi^{n+1} = \Psi^n + \frac{\delta t}{G}\nabla\cdot\left\{-\boldsymbol{V}^{n+1/2}\Psi^n + \frac{\delta t}{2G}\boldsymbol{V}^{n+1/2}\nabla\cdot\left(\boldsymbol{V}^{n+1/2}\Psi^n\right) + \boldsymbol{H}_X\right\} + O^4(\delta t, \boldsymbol{\delta x}) \ , \tag{A.8}$$

$$\begin{aligned}\boldsymbol{H}_X = {} & \boldsymbol{H}_{UPW} + \frac{\boldsymbol{\delta x}}{2}\odot\left\lceil\overline{\boldsymbol{V}}^{n+1/2,\,n}\right\rceil\odot\nabla\Psi^n + \frac{\delta t}{2}\boldsymbol{\delta x}\odot\left\lceil\boldsymbol{V}^{n+1/2}\right\rceil\odot\nabla\left[\frac{1}{G}\nabla\cdot\left(\boldsymbol{V}^{n+1/2}\Psi^n\right)\right] \\ & - \frac{\delta t^2}{2G}\boldsymbol{V}^{n+1/2}\nabla\cdot\left[\frac{\boldsymbol{V}^{n+1/2}}{G}\nabla\cdot\left(\boldsymbol{V}^{n+1/2}\Psi^n\right)\right].\end{aligned} \tag{A.9}$$

A.2. Expansion in time

After expanding (A.8) in time about a common time level t^n and again omitting the corresponding index we obtain

$$\Psi + \delta t\frac{\partial\Psi}{\partial t} + \frac{\delta t^2}{2}\frac{\partial^2\Psi}{\partial t^2} + \frac{\delta t^3}{6}\frac{\partial^3\Psi}{\partial t^3} = \Psi + \frac{\delta t}{G}\nabla\cdot\left\{-\boldsymbol{V}\Psi - \frac{\delta t}{2}\frac{\partial\boldsymbol{V}}{\partial t}\Psi + \frac{\delta t}{2G}\boldsymbol{V}\nabla\cdot(\boldsymbol{V}\Psi) + \boldsymbol{H}_{TX}\right\} + O^4(\delta t, \boldsymbol{\delta x}) \ , \tag{A.10}$$

$$\boldsymbol{H}_{TX} = \widetilde{\boldsymbol{H}_X} - \frac{\delta t^2}{8}\frac{\partial^2\boldsymbol{V}}{\partial t^2}\Psi + \frac{\delta t^2}{4G}\frac{\partial\boldsymbol{V}}{\partial t}\nabla\cdot(\boldsymbol{V}\Psi) + \frac{\delta t^2}{4G}\boldsymbol{V}\nabla\cdot\left(\frac{\partial\boldsymbol{V}}{\partial t}\Psi\right) \ , \tag{A.11}$$

where $\widetilde{\boldsymbol{H}_X}$ refers to (A.9) after time expansion that, for high order terms, amounts to replacing $\boldsymbol{V}^{n+1/2}$ with $\boldsymbol{V}^n$ and $\overline{\boldsymbol{V}}^{n+1/2,\,n}$ with $\overline{\boldsymbol{V}}^{n,\,n}$.

Finally, by dividing both sides of (A.10) by δt and rearranging we get the modified equation of MPDATA

$$\frac{\partial\Psi}{\partial t} = \frac{1}{G}\nabla\cdot\left\{-\boldsymbol{V}\Psi - \frac{\delta t}{2}\frac{\partial\boldsymbol{V}}{\partial t}\Psi + \frac{\delta t}{2G}\boldsymbol{V}\nabla\cdot(\boldsymbol{V}\Psi) + \boldsymbol{H}_{TX}\right\} - \frac{\delta t}{2}\frac{\partial^2\Psi}{\partial t^2} - \frac{\delta t^2}{6}\frac{\partial^3\Psi}{\partial t^3} + O^3(\delta t, \boldsymbol{\delta x}). \tag{A.12}$$

A.3. Expressing temporal derivatives in terms of spatial derivatives

In order to express the rhs of (A.12) solely in terms of the spatial derivatives of the scalar Ψ we have to relate the second and the third temporal derivative of Ψ to the spatial derivatives. First, we observe that as the second temporal derivative on the rhs of (A.12) is multiplied by δt and the third is multiplied by δt^2, it is sufficient to know them up to $O^2(\delta t, \boldsymbol{\delta x})$ and $O^1(\delta t, \boldsymbol{\delta x})$, respectively. Keeping this in mind, we start by differentiating both sides of (A.12) with respect to time to obtain

$$\begin{aligned}\frac{\partial^2\Psi}{\partial t^2} = \frac{1}{G}\nabla\cdot\Bigg\{ & -\frac{\partial\boldsymbol{V}}{\partial t}\Psi - \boldsymbol{V}\frac{\partial\Psi}{\partial t} - \frac{\delta t}{2}\frac{\partial^2\boldsymbol{V}}{\partial t^2}\Psi - \frac{\delta t}{2}\frac{\partial\boldsymbol{V}}{\partial t}\frac{\partial\Psi}{\partial t} \\ & + \frac{\delta t}{2G}\frac{\partial\boldsymbol{V}}{\partial t}\nabla\cdot(\boldsymbol{V}\Psi) + \frac{\delta t}{2G}\boldsymbol{V}\nabla\cdot\left(\frac{\partial\boldsymbol{V}}{\partial t}\Psi\right) + \frac{\delta t}{2G}\boldsymbol{V}\nabla\cdot\left(\boldsymbol{V}\frac{\partial\Psi}{\partial t}\right)\Bigg\} - \frac{\delta t}{2}\frac{\partial^3\Psi}{\partial t^3} + O^2(\delta t, \boldsymbol{\delta x}).\end{aligned} \tag{A.13}$$

By using (A.12) on the rhs of (A.13) we get

$$\frac{\partial^2 \Psi}{\partial t^2} = \frac{1}{G}\nabla \cdot \Bigg\{ -\frac{\partial \boldsymbol{V}}{\partial t}\Psi + \frac{\boldsymbol{V}}{G}\nabla\cdot(\boldsymbol{V}\Psi) - \frac{\delta t}{2}\frac{\partial^2 \boldsymbol{V}}{\partial t^2}\Psi - \frac{\delta t}{G}\boldsymbol{V}\nabla\cdot\left[\frac{\boldsymbol{V}}{G}\nabla\cdot(\boldsymbol{V}\Psi)\right] + \frac{\delta t}{2}\boldsymbol{V}\frac{\partial^2 \Psi}{\partial t^2} + \frac{\delta t}{G}\frac{\partial \boldsymbol{V}}{\partial t}\nabla\cdot(\boldsymbol{V}\Psi) + \frac{\delta t}{G}\boldsymbol{V}\nabla\cdot\left(\frac{\partial \boldsymbol{V}}{\partial t}\Psi\right)\Bigg\} - \frac{\delta t}{2}\frac{\partial^3 \Psi}{\partial t^3} + O^2(\delta t, \boldsymbol{\delta x}) \; . \tag{A.14}$$

After applying (A.14) to the rhs of itself we have

$$\frac{\partial^2 \Psi}{\partial t^2} = \frac{1}{G}\nabla \cdot \Bigg\{ -\frac{\partial \boldsymbol{V}}{\partial t}\Psi + \frac{\boldsymbol{V}}{G}\nabla\cdot(\boldsymbol{V}\Psi) - \frac{\delta t}{2}\frac{\partial^2 \boldsymbol{V}}{\partial t^2}\Psi - \frac{\delta t}{2G}\boldsymbol{V}\nabla\cdot\left[\frac{\boldsymbol{V}}{G}\nabla\cdot(\boldsymbol{V}\Psi)\right] + \frac{\delta t}{G}\frac{\partial \boldsymbol{V}}{\partial t}\nabla\cdot(\boldsymbol{V}\Psi) + \frac{\delta t}{2G}\boldsymbol{V}\nabla\cdot\left(\frac{\partial \boldsymbol{V}}{\partial t}\Psi\right)\Bigg\} - \frac{\delta t}{2}\frac{\partial^3 \Psi}{\partial t^3} + O^2(\delta t, \boldsymbol{\delta x}). \tag{A.15}$$

By differentiating both sides of (A.15) with respect to time and using the order argument again we obtain

$$\frac{\partial^3 \Psi}{\partial t^3} = \frac{1}{G}\nabla \cdot \Bigg\{ -\frac{\partial^2 \boldsymbol{V}}{\partial t^2}\Psi - \frac{\partial \boldsymbol{V}}{\partial t}\frac{\partial \Psi}{\partial t} + \frac{1}{G}\frac{\partial \boldsymbol{V}}{\partial t}\nabla\cdot(\boldsymbol{V}\Psi) + \frac{\boldsymbol{V}}{G}\nabla\cdot\left(\frac{\partial \boldsymbol{V}}{\partial t}\Psi\right) + \frac{\boldsymbol{V}}{G}\nabla\cdot\left(\boldsymbol{V}\frac{\partial \Psi}{\partial t}\right)\Bigg\} + O^1(\delta t, \boldsymbol{\delta x}). \tag{A.16}$$

Using (A.12) on the rhs of (A.16) leads to

$$\frac{\partial^3 \Psi}{\partial t^3} = \frac{1}{G}\nabla \cdot \Bigg\{ -\frac{\partial^2 \boldsymbol{V}}{\partial t^2}\Psi + \frac{2}{G}\frac{\partial \boldsymbol{V}}{\partial t}\nabla\cdot(\boldsymbol{V}\Psi) + \frac{\boldsymbol{V}}{G}\nabla\cdot\left(\frac{\partial \boldsymbol{V}}{\partial t}\Psi\right) - \frac{\boldsymbol{V}}{G}\nabla\cdot\left[\frac{\boldsymbol{V}}{G}\nabla\cdot(\boldsymbol{V}\Psi)\right]\Bigg\} + O^1(\delta t, \boldsymbol{\delta x}). \tag{A.17}$$

By applying first (A.15) and then (A.17) to the rhs of (A.12) we are left with

$$\frac{\partial \Psi}{\partial t} = \frac{1}{G}\nabla\cdot\{-\boldsymbol{V}\Psi + \boldsymbol{H}_{XX}\} + O^3(\delta t, \boldsymbol{\delta x}), \tag{A.18}$$

$$\boldsymbol{H}_{XX} = \boldsymbol{H}_{TX} + \frac{\delta t^2}{6}\frac{\partial^2 \boldsymbol{V}}{\partial t^2}\Psi - \frac{\delta t^2}{3G}\frac{\partial \boldsymbol{V}}{\partial t}\nabla\cdot(\boldsymbol{V}\Psi) - \frac{\delta t^2}{6G}\boldsymbol{V}\nabla\cdot\left(\frac{\partial \boldsymbol{V}}{\partial t}\Psi\right) + \frac{\delta t^2}{6G}\boldsymbol{V}\nabla\cdot\left[\frac{\boldsymbol{V}}{G}\nabla\cdot(\boldsymbol{V}\Psi)\right] \; . \tag{A.19}$$

Finally, the definition $\overline{\overline{\boldsymbol{V}}} := \boldsymbol{H}_{XX}/\Psi$ leads to the final result (12) with $\alpha = 1$, $\beta_M = 1$ and $\gamma = 1$.

[1] R. D. Richtmyer, K. W. Morton, Difference methods for initial-value problems. Second edition (1967).

[2] E. F. Toro, Riemann solvers and numerical methods for fluid dynamics: a practical introduction. Third edition (2009).

[3] D. A. Knoll, L. Chacon, L. G. Margolin, V. A. Mousseau, On balanced approximations for time intergation of multiple time scale systems, J. Comput. Phys. 185 (2003) 583–611. doi:10.1016/S0021-9991(03)00008-1.

[4] D. Jarecka, A. Jaruga, P. K. Smolarkiewicz, A spreading drop of shallow water, J. Comput. Phys. 289 (2015) 53–61. doi:10.1016/j.jcp.2015.02.003.

[5] P. J. Roache, Computational Fluid Dynamics (1972).

[6] H.-O. Kreiss, J. Oliger, Comparison of accurate methods for the integration of hyperbolic equations, Tellus 24 (1972) 199–215. doi:10.1111/j.2153-3490.1972.tb01547.x.

[7] A. Jaruga, S. Arabas, D. Jarecka, H. Pawlowska, P. K. Smolarkiewicz, M. Waruszewski, libmpdata++ 1.0: a library of parallel MPDATA solvers for systems of generalised transport equations, Geosci. Model Dev. 8 (2015) 1005–1032. doi:10.5194/gmd-8-1005-2015.

[8] Z. J. Wang, K. Fidkowski, R. Abgrall, F. Bassi, D. Caraeni, A. Cary, H. Deconinck, R. Hartmann, K. Hillewaert, H. T. Huynh, et al., High-order CFD methods: current status and perspective, Int. J. Numer. Methods Fluids 72 (2013) 811–845. doi:10.1002/fld.3767.

[9] P. A. Ullrich, Understanding the treatment of waves in atmospheric models. Part 1: The shortest resolved waves of the 1D linearized shallow-water equations, Q. J. R. Meteorol. Soc. 140 (2014) 1426–1440. doi:10.1002/qj.2226.

[10] P. A. Ullrich, C. Jablonowski, MCore: A non-hydrostatic atmospheric dynamical core utilizing high-order finite-volume methods, J. Comput. Phys. 231 (2012) 5078–5108. doi:10.1016/j.jcp.2012.04.024.

[11] J. F. Kelly, F. X. Giraldo, Continuous and discontinuous Galerkin methods for a scalable three-dimensional nonhydrostatic atmospheric model: Limited-area mode, J. Comput. Phys. 231 (2012) 7988–8008. doi:10.1016/j.jcp.2012.04.042.

[12] W. C. Skamarock, J. B. Klemp, M. G. Duda, L. D. Fowler, S.-H. Park, T. D. Ringler, A multiscale nonhydrostatic atmospheric model using centroidal Voronoi tesselations and C-grid staggering, Mon. Weather Rev. 140 (2012) 3090–3105. doi:10.1175/MWR-D-11-00215.1.

[13] P. K. Smolarkiewicz, A fully multidimensional positive definite advection transport algorithm with small implicit diffusion, J. Comput. Phys. 54 (1984) 325–362. doi:10.1016/0021-9991(84)90121-9.

[14] P. K. Smolarkiewicz, L. G. Margolin, MPDATA: A finite-difference solver for geophysical flows, J. Comput. Phys. 140 (1998) 459–480. doi:10.1006/jcph.1998.5901.

[15] P. K. Smolarkiewicz, J. Szmelter, MPDATA: An edge-based unstructured-grid formulation, J. Comput. Phys. 206 (2005) 624–649. doi:10.1016/j.jcp.2004.12.021.

[16] C. Kühnlein, P. K. Smolarkiewicz, An unstructured-mesh finite-volume MPDATA for compressible atmospheric dynamics, J. Comput. Phys. 334 (2017) 16–30. doi:10.1016/j.jcp.2016.12.054.

[17] P. K. Smolarkiewicz, W. W. Grabowski, The multidimensional positive definite advection transport algorithm: Nonoscillatory option, J. Comput. Phys. 86 (1990) 355–375. doi:10.1016/0021-9991(90)90105-A.

[18] P. Lax, B. Wendroff, Systems of conservation laws, Commun. Pure Appl. Math. 13 (1960) 217–237. doi:10.1002/cpa.3160130205.

[19] P. K. Smolarkiewicz, L. G. Margolin, On forward-in-time differencing for fluids: Extension to a curvilinear framework, Mon. Weather Rev. 121 (1993) 1847–1859. doi:10.1175/1520-0493(1993)121<1847:OFITDF>2.0.CO;2.

[20] L. G. Margolin, P. K. Smolarkiewicz, Z. Sorbjan, Large-eddy simulations of convective boundary layers using nonoscillatory differencing, Physica D 133 (1999) 390–397. doi:10.1016/S0167-2789(99)00083-4.

[21] L. G. Margolin, P. K. Smolarkiewicz, A. A. Wyszogrodzki, Implicit turbulence modeling for high Reynolds number flows, J. Fluids Eng. 124 (2002) 862–867. doi:10.1115/1.1514210.

[22] L. G. Margolin, W. J. Rider, A rationale for implicit turbulence modelling, Int. J. Numer. Methods Fluids 39 (2002) 821–841. doi:10.1002/fld.331.

[23] J. A. Domaradzki, Z. Xiao, P. K. Smolarkiewicz, Effective eddy viscosities in implicit large eddy simulations of turbulent flows, Phys. Fluids 15 (2003) 3890–3893. doi:10.1063/1.1624610.

[24] L. G. Margolin, P. K. Smolarkiewicz, A. A. Wyszogradzki, Dissipation in implicit turbulence models: A computational study, J. Appl. Mech. 73 (2006) 469–473. doi:10.1115/1.2176749.

[25] L. G. Margolin, W. J. Rider, F. F. Grinstein, Modeling turbulent flow with implicit LES, J. Turb. 7 (2006) 1–27. doi:10.1080/14685240500331595.

[26] A. Strugarek, P. Beaudoin, A. S. Brun, P. Charbonneau, S. Mathis, P. K. Smolarkiewicz, Modeling turbulent stellar convection zones: Sub-grid scales effects, Adv. Space Res. 58 (2016) 1538–1553. doi:10.1016/j.asr.2016.05.043.

[27] A. Warn-Varnas, J. Hawkins, P. K. Smolarkiewicz, S. A. Chin-Bing, D. King, Z. Hallock, Solitary wave effects north of Strait of Messina, Ocean Model. 18 (2007) 97–121. doi:10.1016/j.ocemod.2007.03.003.

[28] J. M. Prusa, P. K. Smolarkiewicz, A. A. Wyszogrodzki, EULAG, a computational model for multiscale flows, Comput. Fluids 37 (2008) 1193–1207. doi:10.1016/j.compfluid.2007.12.001.

[29] Z. P. Piotrowski, P. K. Smolarkiewicz, S. P. Malinowski, A. A. Wyszogrodzki, On numerical realizability of thermal convection, J. Comput. Phys. 228 (2009) 6268–6290. doi:10.1016/j.jcp.2009.05.023.

[30] M. Ghizaru, P. Charbonneau, P. K. Smolarkiewicz, Magnetic cycles in global large-eddy simulations of solar convection, Astrophys. J. Lett. 715 (2010) L133–L137. doi:10.1088/2041-8205/715/2/L133.

[31] É. Racine, P. Charbonneau, M. Ghizaru, A. Bouchat, P. K. Smolarkiewicz, On the mode of dynamo action in a global large-eddy simulation of solar convection, Astrophys. J. 735 (2011) 46–67. doi:10.1088/0004-637X/735/1/46.

[32] D. Kumar, R. Bhattacharyya, P. K. Smolarkiewicz, Repetitive formation and decay of current sheets in magnetic loops: An origin of diverse magnetic structures, Phys. Plasmas 22 (2015) 012902. doi:10.1063/1.4905643.

[33] J.-F. Cossette, P. Charbonneau, P. K. Smolarkiewicz, M. P. Rast, Magnetically modulated heat transport in a global simulation of solar magneto-convection, Astrophys. J. 841 (2017) 65–81. doi:10.3847/1538-4357/aa6d60.

[34] P. K. Smolarkiewicz, C. Kühnlein, N. P. Wedi, A consistent framework for discrete integrations of soundproof and compressible PDEs of atmospheric dynamics, J. Comput. Phys. 263 (2014) 185–205. doi:10.1016/j.jcp.2014.01.031.

[35] P. K. Smolarkiewicz, P. Charbonneau, EULAG, a computational model for multiscale flows: An MHD extension, J. Comput. Phys. 236 (2013) 608–623. doi:10.1016/j.jcp.2012.11.008.

[36] P. K. Smolarkiewicz, W. Deconinck, M. Hamrud, C. Kühnlein, G. Mozdzynski, J. Szmelter, N. P. Wedi, A finite-volume module for simulating global all-scale atmospheric flows, J. Comput. Phys. 314 (2016) 287–304. doi:10.1016/j.jcp.2016.03.015.

[37] P. K. Smolarkiewicz, C. Kühnlein, W. W. Grabowski, A finite-volume module for cloud-resolving simulations of global atmospheric flows, J. Comput. Phys. 341 (2017) 208–229. doi:10.1016/j.jcp.2017.04.008.

[38] L. Margolin, P. K. Smolarkiewicz, Antidiffusive velocities for multipass donor cell advection, SIAM J. Sci. Comput. 20 (1998) 907–929. doi:10.1137/S106482759324700X.

[39] R. D. Nair, C. Jablonowski, Moving vortices on the sphere: A test case for horizontal advection problems, Mon. Weather Rev. 136 (2008) 699–711. doi:10.1175/2007MWR2105.1.

[40] P. H. Lauritzen, W. C. Skamarock, M. J. Prather, M. A. Taylor, A standard test case suite for two-dimensional linear transport on the sphere, Geosci. Model Dev. 5 (2012) 887–901. doi:10.5194/gmd-5-887-2012.

[41] D. Drikakis, P. K. Smolarkiewicz, On spurious vortical structures, J. Comput. Phys. 172 (2001) 309–325. doi:10.1006/jcph.2001.6825.

[42] D. Drikakis, L. Margolin, P. K. Smolarkiewicz, On 'spurious' eddies, Int. J. Numer. Methods Fluids 40 (2002) 313–322. doi:10.1002/fld.288.

[43] R. F. Warming, B. J. Hyett, The modified equation approach to the stability and accuracy analysis of finite-difference methods, J. Comput. Phys. 14 (1974) 159–179. doi:10.1016/0021-9991(74)90011-4.

[44] C. Kühnlein, P. K. Smolarkiewicz, A. Dörnbrack, Modelling atmospheric flows with adaptive moving meshes, J. Comput. Phys. 231 (2012) 2741–2763. doi:10.1016/j.jcp.2011.12.012.

[45] P. J. Roache, Code verification by the method of manufactured solutions, J. Fluids Eng. 124 (2002) 4–10. doi:10.1115/1.1436090.

[46] J. Pudykiewicz, Simulation of the Chernobyl dispersion with a 3-D hemispheric tracer model, Tellus B 41 (1989) 391–412. doi:10.1111/j.1600-0889.1989.tb00317.x.

[47] W. Hundsdorfer, B. Koren, van Loon M., J. G. Verwer, A positive finite-difference advection scheme, J. Comput. Phys. 117 (1995) 35–46. doi:10.1006/jcph.1995.1042.

[48] L. M. Frohn, J. H. Christensen, J. Brandt, Development of a high-resolution nested air pollution model: The numerical approach, J. Comput. Phys. 179 (2002) 68–94. doi:10.1006/jcph.2002.7036.

[49] G. R. Carmichael, A. Sandu, T. Chai, D. N. Daescu, E. M. Constantinescu, Y. Tang, Predicting air quality: Improvements through advanced methods to integrate models and measurements, J. Comput. Phys. 227 (2008) 3540–3571. doi:10.1016/j.jcp.2007.02.024.

[50] J. B. White III, J. J. Dongarra, High-performance high-resolution semi-Lagrangian tracer transport on a sphere, J. Comput. Phys. 230 (2011) 6778–6799. doi:10.1016/j.jcp.2011.05.008.

[51] M. Santillana, L. Zhang, R. Yantosca, Estimating numerical errors due to operator splitting in global atmospheric chemistry models: Transport and chemistry, J. Comput. Phys. 305 (2016) 372–386. doi:10.1016/j.jcp.2015.10.052.

[52] J. A. Pudykiewicz, Application of adjoint tracer transport equations for evaluating source parameters, Atmos. Environ. 32 (1998) 3039–3050. doi:10.1016/S1352-2310(97)00480-9.

[53] J. Szmelter, P. K. Smolarkiewicz, An edge-based unstructured mesh discretisation in geospherical framework, J. Comput. Phys. 229 (2010) 4980–4995. doi:10.1016/j.jcp.2010.03.017.

[54] P. H. Lauritzen, P. A. Ullrich, C. Jablonowski, P. A. Bosler, D. Calhoun, A. J. Conley, T. Enomoto, L. Dong, S. Dubey, O. Guba, et al., A standard test case suite for two-dimensional linear transport on the sphere: results from a collection of state-of-the-art schemes, Geosci. Model Dev. 7 (2014) 105–145. doi:10.5194/gmd-7-105-2014.

[55] P. H. Lauritzen, J. Thuburn, Evaluating advection/transport schemes using interrelated tracers, scatter plots and numerical mixing diagnostics, Q. J. R. Meteorol. Soc. 138 (2012) 906–918. doi:10.1002/qj.986.

[56] P. K. Smolarkiewicz, Multidimensional positive definite advection transport algorithm: An overview, Int. J. Numer. Methods Fluids 50 (2006) 1123–1144. doi:10.1002/fld.1071.

[57] P. P. Sullivan, E. G. Patton, The effect of mesh resolution on convective boundary layer statistics and structures generated by large-eddy simulation, Journal of the Atmospheric Sciences 68 (2011) 2395–2415. doi:10.1175/JAS-D-10-05010.1.

[58] S. B. Pope, Turbulent Flows (2000).

[59] P. K. Smolarkiewicz, J. Szmelter, A. A. Wyszogrodzki, An unstructured-mesh atmospheric model for nonhydrostatic dynamics, J. Comput. Phys. 254 (2013) 184–199. doi:10.1016/j.jcp.2013.07.027.

[60] H. Schmidt, U. Schumann, Coherent structure of the convective boundary layer derived from large-eddy simulations, J. Fluid. Mech. 200 (1989) 511–562. doi:10.1017/S0022112089000753.

[61] D. L. Brown, M. L. Minion, Performance of under-resolved two-dimensional incompressible flows simulations, J. Comput. Phys. 122 (1995) 165–183. doi:10.1006/jcph.1995.1205.

[62] M. L. Minion, D. L. Brown, Performance of under-resolved two-dimensional incompressible flows simulations II, J. Comput. Phys. 138 (1997) 734–765. doi:10.1006/jcph.1997.5843.